

1 **The LRRK2 G2019S mutation alters astrocyte-to-neuron communication via**
2 **extracellular vesicles and induces neuron atrophy in a human iPSC-derived**
3 **model of Parkinson's disease**

4

5 Aurelie de Rus Jacquet^{1*}, Jenna L. Tancredi¹, Andrew L. Lemire¹, Michael C. DeSantis¹, Wei-
6 Ping Li¹, Erin K. O'Shea^{1*}

7 ¹Janelia Research Campus, Howard Hughes Medical Institute, Ashburn, VA, 20147

8 *Co-corresponding authors: Aurelie de Rus Jacquet : aureliederus@gmail.com; Erin O'Shea :
9 osheae@hhmi.org

10

11

12

13 **Abstract**

14 Astrocytes are essential cells of the central nervous system, characterized by dynamic
15 relationships with neurons that range from functional metabolic interactions and regulation of
16 neuronal firing activities, to the release of neurotrophic and neuroprotective factors. In
17 Parkinson's disease (PD), dopaminergic neurons are progressively lost during the course of the
18 disease, but the effects of PD on astrocytes and astrocyte-to-neuron communication remains
19 largely unknown. This study focuses on the effects of the PD-related mutation LRRK2 G2019S
20 in astrocytes, generated from patient-derived induced pluripotent stem cells. We report the
21 alteration of extracellular vesicle (EV) biogenesis in astrocytes, and we identify the abnormal
22 accumulation of key PD-related proteins within multi vesicular bodies (MVBs). We found that
23 dopaminergic neurons internalize astrocyte-secreted EVs but LRRK2 G2019S EVs are
24 abnormally enriched in neurites and provide only marginal neurotrophic support to dopaminergic
25 neurons. Thus, dysfunctional astrocyte-to-neuron communication via altered EV biological
26 properties may participate in the progression of PD.

27

28

1 Introduction

2 The loss of dopaminergic neurons in the *substantia nigra pars compacta* is associated with the
3 severe and debilitating motor dysfunction observed in Parkinson's disease (PD) patients
4 (Massano & Bhatia, 2012). The cause of dopaminergic neuron degeneration has been under
5 intense investigation and has revealed the roles played by cellular stressors such as oxidative
6 stress, mitochondrial dysfunction and disruption of protein degradation pathways (Dawson &
7 Dawson, 2003; Lynch-Day, Mao, Wang, Zhao, & Klionsky, 2012). The dysregulation of these
8 pathways within the neurons themselves represent cell-autonomous mechanisms of
9 neurodegeneration, but neurons exist in a highly dynamic multicellular environment in which
10 non-neuronal cells may also contribute to neuron loss (Allen & Lyons, 2018; Liddelow & Barres,
11 2017). Among these non-neuronal populations, astrocytes are specialized in detecting and
12 responding to neuronal signals to support their health and function (Allen & Eroglu, 2017;
13 Banker, 1980), suggesting that impaired astrocytic functions could initiate or accelerate neuron
14 loss. Neurons rely on astrocytes for regulation of their firing activities (Deemyad, Luthi, &
15 Spruston, 2018), for trophic and metabolic support (Allen & Lyons, 2018), and detoxification of
16 harmful factors (Ioannou et al., 2019). However, astrocytes can change from a resting to a
17 reactive state in response to injury (Zamanian et al., 2012) or normal aging (Clarke et al., 2018).
18 In fact, depending on the nature of the extracellular signals released after injury, astrocytes can
19 protect neurons or induce neurotoxicity (Liddelow et al., 2017; Zamanian et al., 2012). The role
20 of astrocytes in promoting neuron loss has been the focus of a number of studies across
21 multiple neurodegenerative diseases including ALS (Di Giorgio, Boulting, Bobrowicz, & Eggan,
22 2008; Haidet-Phillips et al., 2011), Huntington disease (Valenza et al., 2015), and PD (di
23 Domenico et al., 2019; X. L. Gu et al., 2010). For example, studies showed that astrocytes with
24 the ALS-causing mutation SOD1 G93A produced factors toxic to motor neurons (Di Giorgio et
25 al., 2008), as well as failed to secrete factors that support the viability of neurons (Basso et al.,
26 2013). These observations suggest that disease astrocytes undergo important functional
27 changes that ultimately affect the viability of neurons. The consequences of PD-related
28 mutations in the functionality of astrocytes and their ability to support neuronal survival are
29 unclear, and much remains to be discovered to fully appreciate the unique contributions of
30 astrocytes to PD pathogenesis.

31 Cell-to-cell communication refers to the exchange of information between two or more cells, and
32 is mediated by several tightly regulated mechanisms including the secretion of signaling factors
33 directly into the extracellular space or enclosed within extracellular vesicles (EVs). While
34 astrocyte paracrine signaling via the secretion of soluble factors into the extracellular space has
35 been the focus of many studies (Allen & Eroglu, 2017; Spampinato, Bortolotto, Canonico,
36 Sortino, & Grilli, 2019), astrocyte communication via secreted EVs has not been well
37 characterized. EVs represent a heterogeneous population of vesicles that can be further
38 classified into different subtypes according to their size, biogenesis pathways and cargo.
39 Microvesicles (~ 100 nm-1 μ m diameter) are formed by budding of the plasma membrane
40 directly into the extracellular space, and their cargo resembles the cytoplasmic signature of the
41 cell of origin (Pegtel & Gould, 2019). Exosomes (~ 40-120 nm) are formed by a tightly regulated
42 inward budding of early endosomes to form exosome-containing multi vesicular bodies (MVBs),
43 as well as by budding of the plasma membrane (Pegtel & Gould, 2019). The sorting and loading

1 of exosome cargo is an active and regulated process (Temoche-Diaz et al., 2019), and the
2 regulatory factors involved in EV/exosome biogenesis are just beginning to be identified.
3 Accumulating evidence suggests that the PD-related protein LRRK2 plays a role in vesicle
4 trafficking, possibly via phosphorylation of Rab GTPase substrates (Alessi & Sammler, 2018;
5 Steger et al., 2016). The PD-causing mutation G2019S occurs within the kinase domain of
6 LRRK2, resulting in a hyper-active kinase form (West et al., 2005), which could affect the
7 MVB/EV pathway. Furthermore, the nature of the EV cargo varies in health and disease
8 (Chaudhuri et al., 2018; Lamontagne-Proulx et al., 2019). The composition of EVs isolated from
9 the biofluids of PD patients is different from that of healthy controls (Fraser, Rawlins, et al.,
10 2016; Lamontagne-Proulx et al., 2019; Shi et al., 2014), and they contain proteins associated
11 with PD, such as LRRK2 and alpha-synuclein (α Syn). The clinical observation that the EV
12 profile is altered in PD patients, and the proposed role of LRRK2 in vesicle trafficking, open
13 exciting opportunities to further investigate the relationships between EVs and PD pathogenesis
14 in disease-relevant cell types.

15 Here we made use of human-based genetic model of PD using induced pluripotent stem cells
16 (iPSCs) derived from PD patients with the LRRK2 G2019S mutation and its gene-corrected
17 isogenic control (Reinhardt et al., 2013). The LRRK2 G2019S mutation is one of the most
18 common genetic determinants associated with an increased risk to develop sporadic or familial
19 PD (Bonifati, 2006; Kumari & Tan, 2009). We show that the LRRK2 G2019S mutation alters the
20 phenotype of MVBs and secreted EVs by affecting the morphology and distribution of MVBs, the
21 morphology of secreted EVs, and by over-accumulating the PD-related proteins LRRK2 and
22 phospho-S129 α Syn in MVBs. Importantly, we show that astrocyte-derived EVs are internalized
23 by dopaminergic neurons, and WT but not LRRK2 G2019S EVs support neuronal survival.
24 Overall, this study supports a non-cell autonomous contribution to dopaminergic neuron loss in
25 PD, and suggests pathologic dysregulation of EV-mediated astrocyte-to-neuron communication
26 by the PD-related mutation LRRK2 G2019S.

27

28 **Results**

29 **Differentiation of LRRK2 G2019S iPSCs and gene-corrected isogenic controls into** 30 **neural progenitor cells and astrocytes**

31 We obtained iPSCs reprogrammed from the dermal fibroblasts of patients with the LRRK2
32 G2019S mutation, and gene-corrected isogenic controls (Reinhardt et al., 2013). Karyotyping
33 was carried out regularly to assess the chromosomal integrity of the iPSCs (Supplementary
34 Figure 1A). In contrast to previous studies using control iPSCs derived from an unrelated
35 healthy donor, the disease and control iPSC pairs differ only in a single point mutation in
36 *LRRK2*. This isogenic wild-type control is essential to ensure that the experimental
37 observations are a consequence of the mutation of interest, and do not result from differences in
38 genetic background, or from differences that could arise during fibroblast reprogramming of
39 each non-isogenic pair (Gore et al., 2011; Soldner et al., 2009). Since PD pathology significantly
40 affects the region of the midbrain, we sought to prepare astrocytes from neural progenitor cells
41 (NPCs) patterned toward a midbrain fate. We adapted the protocol developed by Kriks et al. to

1 generate a population of renewable midbrain-patterned NPCs that can differentiate into
2 astrocytes or dopaminergic neurons, depending on exogenous cues (de Rus Jacquet, 2019;
3 Kriks et al., 2011; Tcw et al., 2017). The midbrain and floor plate identity of the NPCs was
4 systematically validated for each iPSC-to-NPC differentiation by RT-qPCR (Supplementary
5 Figure 1B), and the differentiated NPCs expressed characteristic NPC markers such as
6 vimentin, SOX1, nestin, and notch1 (Supplementary Figure 1C). Midbrain-patterned NPCs
7 carrying the LRRK2 G2019S mutation or its isogenic control were differentiated into astrocytes
8 as described previously (de Rus Jacquet, 2019; Tcw et al., 2017). As expected, the astrocytes
9 expressed the markers GFAP, vimentin, and CD44 as demonstrated by immunofluorescence
10 (Figure 1A) and flow cytometry analyses (Supplementary Figure 1D). To further demonstrate
11 the successful differentiation of iPSCs into different cell types, we analyzed gene expression
12 using RNA-sequencing analysis (RNA-seq), including primary human midbrain astrocyte
13 samples in the RNA-seq study to serve as a positive control for human astrocyte identity. PCA
14 and unsupervised cluster analyses separated iPSCs, NPCs and astrocytes into independent
15 clusters (Supplementary Figure 1E-F). Importantly, the transcriptome of iPSC-derived
16 astrocytes showed more similarities to fetal human midbrain astrocytes than to NPCs or iPSCs,
17 validating their astrocyte identity (Supplementary Figure 1F).

18

19 **Expression of exosome components in iPSC-derived astrocytes is altered by the** 20 **LRRK2 G2019S mutation**

21 We analyzed the effects of the LRRK2 G2019S mutation on global gene expression patterns in
22 iPSC-derived astrocytes using RNA-seq analysis. Differential gene expression analysis
23 revealed that the LRRK2 G2019S mutation dysregulated the expression of a total of 752 genes
24 (Figure 1B). Classification of these genes using k-means clustering showed that they are
25 distributed between transcripts expressed at high, moderate and low levels based on their
26 $\log_{10}(1+\text{normalized sequencing counts})$ value, suggesting that LRRK2 G2019S affects a broad
27 range of targets (Figure 1B). Gene ontology (GO) analysis revealed that components of the
28 extracellular compartment are the most up-regulated, and include the cell surface, extracellular
29 matrix and extracellular exosomes (Figure 1D). The exosome component is the most
30 significantly up-regulated GO term and is comprised of a total of 174 genes. The gene products
31 associated with this category are proteins found in exosomes (e.g. CBR1), or proteins
32 associated with exosome biogenesis (e.g. CD82) and trafficking (e.g. Rab27b) (Andreu &
33 Yanez-Mo, 2014; Chiasserini et al., 2014; Ostrowski et al., 2010). Quantification of gene
34 expression by RT-qPCR showed a 5-fold increase in the expression of *Rab27b*, and a 64-fold
35 increase in *CD82*, in LRRK2 G2019S astrocytes compared to WT astrocytes (Figure 1E-F).
36 Thus, the LRRK2 mutation G2019S leads to the significant up-regulation of exosome
37 components in astrocytes.

38

39 **LRRK2 G2019S affects the size of MVBs in iPSC-derived astrocytes**

40 The exosome pathway is characterized by the formation of MVBs, endosome-derived structures
41 that form exosomes via inward budding of the endosomal membrane (Pegtel & Gould, 2019).

1 Using transmission electron microscopy (TEM), we first confirmed that iPSC-derived astrocytes
2 produce MVBs-like structures. We found that while both WT and LRRK2 G2019S astrocytes
3 produce MVBs (Figure 2A), their average size is genotype-dependent. The area of MVBs in
4 LRRK2 G2019S astrocytes is smaller than in WT astrocytes, with an average of $0.26 \mu\text{m}^2$ (SEM
5 = 0.02079) in LRRK2 G2019S and $0.44 \mu\text{m}^2$ (SEM = 0.03472) in WT cells (Figure 2B). MVBs
6 with an area smaller than $0.2 \mu\text{m}^2$ are over-represented in LRRK2 G2019S compared to WT
7 astrocytes, which range in area from 0.1 to $1.2 \mu\text{m}^2$ (Figure 2C). Tetraspanins are
8 transmembrane proteins, and the tetraspanin CD63 is enriched in exosomes and widely used
9 as an exosomal marker (Escola et al., 1998; Men et al., 2019). However, cell-type specificities in
10 the expression of exosomal markers such as CD63 have been documented (Jorgensen et al.,
11 2013; Yoshioka et al., 2013). We therefore confirmed the presence of CD63-positive MVBs in
12 iPSC-derived astrocytes by immunofluorescence (Figure 2D) and immunogold electron
13 microscopy (IEM) (Figure 2E). IEM images showed the abundance of CD63 localized within
14 MVBs in WT (Figure 2E) and LRRK2 G2019S (not shown) astrocytes, confirming that CD63 is a
15 good marker of MVBs and exosomes in iPSC-derived astrocytes. These results demonstrate
16 morphological defects in the MVBs produced by astrocytes derived from PD patients. Antibodies
17 that target the CD63 protein accurately label astrocytic MVBs, and are therefore valuable
18 markers to further characterize LRRK2 G2019S-dependent alterations in MVB-related
19 pathways.

20

21 **LRRK2 G2019S affects the size of EVs secreted by iPSC-derived astrocytes**

22 The alteration of MVB size and the dysregulated expression of key components involved in
23 MVB trafficking (such as Rab27b) suggests that EV biogenesis in astrocytes may be affected by
24 the G2019S mutation. We therefore investigated if the LRRK2 G2019S mutation could affect the
25 release and morphology of astrocyte-secreted EVs. We first analyzed iPSC-derived astrocytes
26 by TEM and confirmed the presence of EVs that appear to be secreted by exocytosis (Figure
27 3A), and by a mechanism that resembles membrane budding or shedding (Supplementary
28 Figure 2A). We then collected and processed astrocyte conditioned media (ACM) by
29 ultracentrifugation. Successive rounds of ultracentrifugation resulted in the isolation of an EV-
30 enriched pellet, immediately prepared for cryogenic electron microscopy (cryo-EM) or stored for
31 later analysis (Figure 3B). EVs form a heterogeneous population differing in their biogenesis
32 pathway (endosomal or plasma membrane budding) and cargo (Pegtel & Gould, 2019;
33 Temoche-Diaz et al., 2019). The unique characteristics of different EV populations are not fully
34 understood, but the documentation of their size range and molecular signatures are commonly
35 used to describe EV populations. The astrocyte-derived EV pellet is enriched in exosomes, as
36 demonstrated by the expression of 8 exosomal markers and the absence of cellular
37 contamination (Supplementary Figure 2B). Analysis of the EV pellet by ELISA showed a similar
38 number of CD63⁺ exosomes secreted by WT and LRRK2 G2019S astrocytes (Figure 3C). TEM
39 and nanotracking particle analysis are common methods traditionally used to estimate the size
40 distribution of EVs, but their accuracy is often challenged by sample processing artifacts and
41 technical biases (Pegtel & Gould, 2019). To overcome these limitations, we used a cryo-EM
42 approach to analyze the size of EVs secreted by WT and LRRK2 G2019S astrocytes. EVs

1 mostly displayed a circular morphology (as opposed to the cup-shaped morphology observed by
2 TEM) (Figure 3D), but a variety of other shapes were also observed (Supplementary Figure 2C).
3 WT astrocyte-secreted EVs displayed a large range of sizes, from 80 nm to greater than 600 nm
4 in diameter, with a majority of EVs in the 120 - 480 nm range. In contrast, LRRK2 G2019S EVs
5 are over-represented in the 160 - 280 nm diameter range, with only a few EVs smaller than 120
6 nm (Figure 3E). We conclude from these results that astrocytes with the PD-related mutation
7 LRRK2 G2019S do not produce or release the full size range of EVs compared to wild-type
8 astrocytes.

9

10 **LRRK2 is associated with MVBs and EVs in iPSC-derived astrocytes**

11 In light of our observations that mutations in LRRK2 result in altered astrocytic MVB and EV
12 phenotypes, we asked if LRRK2 is directly associated with MVBs in astrocytes and if this
13 association is altered by the LRRK2 G2019S mutation. We analyzed and quantified the co-
14 localization of the MVB marker CD63 with LRRK2 (Figure 4A), and found that the proportion of
15 LRRK2⁺/CD63⁺ structures remains unchanged between WT and LRRK2 G2019S astrocytes
16 (Figure 4B). However, this immunofluorescence analysis does not discriminate between LRRK2
17 signal localized at the periphery or within CD63⁺ structures. To reveal the localization of LRRK2
18 in finer detail, we analyzed IEM images which demonstrated that LRRK2 (small gold) is
19 localized both in the vicinity of and inside CD63⁺ MVBs (large gold) (Figure 4C). Importantly,
20 small gold LRRK2 was more frequently localized inside MVBs in LRRK2 G2019S astrocytes
21 compared to WT astrocytes – 65 % of MVBs in LRRK2 G2019S astrocytes are LRRK2⁺/CD63⁺
22 vs only 44 % in WT astrocytes. LRRK2 G2019S astrocytes contained an average of 1.8 LRRK2
23 small gold particles per MVB compared to only 0.9 small gold particles in WT astrocytes, and
24 MVB populations containing more than 5 LRRK2 small gold particles were only observed in
25 LRRK2 G2019S astrocytes (Figure 4D). We then performed imaging and biochemical analyses
26 to determine if astrocytes secrete LRRK2 in EVs. IEM revealed the co-localization of CD63 and
27 LRRK2 at the plasma membrane (Figure 4E), and ELISA analysis confirmed the presence of
28 LRRK2 in EV-enriched fractions isolated from ACM (Supplementary Figure 3A). We conclude
29 that LRRK2 is associated with MVBs in astrocytes and is secreted in astrocyte-derived EVs, and
30 the PD-related LRRK2 G2019S mutation results in the abnormal accumulation of LRRK2 inside
31 MVBs and EVs.

32

33 **The LRRK2 mutation G2019S alters MVB distribution in iPSC-derived astrocytes**

34 The proposed role of LRRK2 in vesicle trafficking (Alessi & Sammler, 2018; Steger et al., 2016),
35 in addition to the dysregulation of known factors involved in exosome/MVB trafficking in mutant
36 astrocytes (Figure 1E), and accumulation of LRRK2 in mutant MVBs (Figure 4D) suggested that
37 the trafficking or spatial distribution of vesicles could be disrupted in LRRK2 G2019S astrocytes.
38 To gain further insight into the functional role of LRRK2 in the MVB pathway, we used
39 immunofluorescence to probe the spatial distribution of CD63⁺ MVBs in WT and LRRK2
40 G2019S astrocytes (Figure 5A). We measured the distance of CD63⁺ structures to the nucleus
41 and found that CD63⁺ MVBs accumulated primarily in the perinuclear region of WT astrocytes

1 (Figure 5B). In contrast, CD63⁺ MVBs were less clustered near the nucleus in LRRK2 G2019S
2 cells. The median distance of CD63⁺ MVBs to the nuclear membrane was 9.2 μ m in LRRK2
3 G2019S astrocytes compared to 4.8 μ m in WT astrocytes. Furthermore, 75 % of the WT CD63⁺
4 MVBs were localized at a distance to the nucleus smaller than 11.23 μ m, compared to 19.34 μ m
5 in LRRK2 G2019S astrocytes (Figure 5B-C). The observation that LRRK2 G2019S disrupts the
6 perinuclear distribution of CD63⁺ MVBs suggests that their localization is influenced by the
7 LRRK2 protein, and this cellular organization is altered in the astrocytes of PD patients.

8

9 **The LRRK2 G2019S mutation increases the amount of phosphorylated alpha** 10 **synuclein (Ser129) in MVBs**

11 EVs isolated from the biofluids of PD patients exhibit accumulation of α Syn (Lamontagne-Proulx
12 et al., 2019; Shi et al., 2014; Zhao et al., 2018), a hallmark protein whose phosphorylation at the
13 serine residue 129 (p- α Syn) has been associated with accelerated PD pathogenesis (Fujiwara
14 et al., 2002; Gorbatyuk et al., 2008). Since the MVB/EV secretion pathway is altered in our
15 LRRK2 G2019S model of PD, we reasoned that mutant astrocytes might produce α Syn-
16 enriched EVs by accumulating the protein in its native or phosphorylated form in MVBs or EVs.
17 IEM analysis revealed an abundance of p- α Syn (small gold) inside and in the vicinity of MVBs of
18 LRRK2 G2019S iPSC-derived astrocytes, but not WT astrocytes (Figure 6A). We observed that
19 55 % of the CD63⁺ (large gold) MVBs in LRRK2 G2019S astrocytes are also p- α Syn⁺ (small
20 gold), compared to only 16 % in WT MVBs. LRRK2 G2019S astrocytes contained on average
21 1.3 p- α Syn small gold particles per MVB compared to only 0.16 small gold particles in WT
22 astrocytes, and MVB populations containing more than 3 p- α Syn small gold particles were only
23 observed in LRRK2 G2019S astrocytes (Figure 6B). When we analyzed the content of EVs by
24 ELISA, we found that total α Syn levels in EV-enriched fractions are similar between WT and
25 LRRK2 G2019S (Supplementary Figure 3B). These results suggest that astrocytes secrete
26 α Syn-containing EVs, and the LRRK2 G2019S mutation enhances the accumulation of the
27 pathologic p- α Syn in MVB-related astrocyte secretory pathways.

28

29 **Exosomes secreted by iPSC-derived astrocytes are internalized by iPSC-derived** 30 **dopaminergic neurons**

31 EVs have been suggested to mediate astrocyte paracrine signaling and affect neuronal health
32 (Basso et al., 2013; Chaudhuri et al., 2018; Pascua-Maestro et al., 2018); it is therefore
33 important to understand the pattern of astrocyte-derived EV uptake by dopaminergic neurons in
34 health and disease. We investigated the internalization of WT and LRRK2 G2019S astrocyte-
35 derived exosomes by dopaminergic neurons to identify genotype-dependent alterations in
36 astrocyte-to-neuron exosome shuttling. To monitor production of EVs by astrocytes and assess
37 uptake by neurons, we fluorescently labeled exosomes in astrocytes with one color (CD63-GFP)
38 and labeled neurons with a second color (tdTomato). Subsequently, astrocytes and neurons
39 were co-cultured, and the uptake of green-labeled exosomes by dopaminergic neurons was
40 monitored by live-cell confocal microscopy (Figure 7A-B). We produced a 3D reconstitution of
41 neurons and exosomes, and segmented intracellular and extracellular exosomal populations

1 (Figure 7B). We observed the presence of astrocyte-derived exosomes in the somas and
2 neurites of dopaminergic neurons (Figure 7Bvi), and endocytosis of extracellular exosomes
3 (Supplementary Figure 4). We then sought to determine if the efficiency of exosome uptake by
4 dopaminergic neurons was influenced by the astrocyte genotype. We co-cultured dopaminergic
5 neurons with either WT or G2019S astrocytes, but did not observe a difference in the proportion
6 of exosome-containing neurons. On average, 40 % of the dopaminergic neurons had
7 internalized exosomes regardless of the astrocyte genotype (Figure 7C). Although there was no
8 difference in the amount of exosomes internalized by neurons exposed to either WT or LRRK2
9 G2019S astrocytes (Figure 7D), exosomes were significantly over-represented in the neurites of
10 neurons exposed to LRRK2 G2019S astrocytes (Figure 7E). These results show that astrocyte-
11 secreted CD63⁺ exosomes are internalized by neurons, but in the presence of PD astrocytes
12 the pattern of uptake of exosomes is changed, suggesting that the astrocyte-to-neuron shuttling
13 of EV-enclosed proteins may be affected.

14

15 **LRRK2 G2019S iPSC-derived astrocytes induce a non-cell autonomous loss of** 16 **iPSC-derived dopaminergic neurons**

17 To further determine the functional consequences of the LRRK2 G2019S mutation in astrocyte-
18 to-neuron communication, we investigated the impact of WT or LRRK2 G2019S astrocytes on
19 neuronal health. We co-cultured astrocytes and dopaminergic neurons for 14 days and
20 observed a loss of and morphological changes to dopaminergic neurons in presence mutant
21 astrocytes (Figure 8A-B). The neuronal dendrites shortened from an average of 60 μm in WT to
22 45 μm in LRRK2 G2019S cultures (Figure 8C). These results are in agreement with previous
23 observations that LRRK2 G2019S astrocytes induce loss of dopaminergic neurons compared to
24 astrocytes derived from a healthy (non-isogenic) donor (di Domenico et al., 2019). To determine
25 if these morphological changes are mediated by direct contact between astrocytes and neurons
26 or if they rely solely on astrocyte secreted factors, dopaminergic neurons were cultured in ACM
27 prepared from WT or LRRK2 G2019S astrocytes. After 14 days in culture, the average dendrite
28 length of dopaminergic neurons exposed to WT ACM was 64.4 μm , compared to 50.3 μm if the
29 dopaminergic neurons were exposed to basal NB/B27 medium (Figure 8E). This observation
30 suggests that WT ACM, but not basal medium, contains neurotrophic factors necessary for
31 dendrite outgrowth. LRRK2 G2019S ACM mimicked the phenotype observed by direct co-
32 culture, with a 26 % increase in the number of short neurites (0-40 μm), and the absence of long
33 neurites (160-200 μm) compared to neurons exposed to WT ACM (Figure 8F). The average
34 dendrite length of dopaminergic neurons cultured in basal medium or LRRK2 G2019S ACM is
35 equivalent (50.3 μm vs 49.1 μm respectively) (Figure 8E). We conclude from our observations
36 that the morphological atrophy in dopaminergic neurons may result from a lack of neurotrophic
37 support by the LRRK2 G2019S astrocyte secretome.

38

39 **Two distinct secretory pathways contribute to the trophic support of iPSC-** 40 **derived dopaminergic neurons by WT but not LRRK2 G2019S iPSC-derived** 41 **astrocytes**

1 The astrocyte secretome comprises factors directly secreted into the medium as well as factors
2 enclosed in EVs. We therefore assessed the neurotrophic potential of EVs vs EV-free medium
3 prepared from WT or LRRK2 G2019S astrocytes. We collected ACM and prepared EV-free and
4 EV-enriched fractions using sequential ultracentrifugation (Figure 3B). Dopaminergic neurons
5 were cultured for 14 days in basal medium, or EV-free medium prepared from WT or LRRK2
6 G2019S astrocytes. WT EV-free medium promoted neuronal health, as evidenced by an
7 average dendrite outgrowth of 60.3 μm compared to 51 μm in basal medium (Figure 9A). In
8 contrast, LRRK2 G2019S EV-free medium did not support dendrite outgrowth, as evidenced by
9 an average length of 48.7 μm . The analysis of the distribution of dendrite lengths shows a
10 greater proportion of short neurites (0-40 μm) in dopaminergic neurons exposed to basal
11 medium or LRRK2 G2019S EV-free medium (Figure 9B). We conclude that WT but not LRRK2
12 G2019S ACM mediates neuron growth.

13 To test the hypothesis that astrocytes shuttle trophic factors to neurons via EVs, we cultured
14 dopaminergic neurons with basal medium, or with WT or LRRK2 G2019S EV-enriched fractions.
15 WT EVs supported a 30 % increase in dendrite length compared to basal medium (Figure 9C),
16 which is higher than the 18 % increase supported by WT soluble factors (Figure 9A).
17 Interestingly, LRRK2 G2019S EVs were not as efficient as their WT counterparts, but they
18 supported an 11 % increase in dendrite length (Figure 9C) and reduced the proportion of short
19 neurites (0-40 μm) (Figure 9D). These results suggest that WT astrocytes secrete neurotrophic
20 factors not only via direct release in the extracellular compartment, but also via production and
21 release of EVs. Supplementation of the neuronal basal medium with WT or LRRK2 G2019S
22 EVs resulted in neuron growth, but LRRK2 G2019S EVs provided only a marginal trophic
23 support compared to WT EVs. Together with the previous observation that LRRK2 G2019S
24 affects the biogenesis of EVs in astrocytes and the distribution of internalized EVs in neurons,
25 these data support a model of astrocyte-to-neuron trophic support via EV-mediated shuttling of
26 factors, and this system appears to be dysregulated in the LRRK2 G2019S model of PD.

27

28 Discussion

29 Dysregulation of iPSC-derived astrocyte-mediated EV biogenesis in Parkinson's 30 disease

31 Here we document the dysregulation of the MVB-mediated secretory pathway in human iPSC-
32 derived astrocytes containing the PD-related mutation LRRK2 G2019S. Transcriptomic profiling
33 revealed the misregulation of expression of exosome components in LRRK2 G2109S vs WT
34 astrocytes (Figure 1). We found that genes involved in aspects of MVB trafficking and EV
35 biogenesis, including *Rab27b*, were overexpressed in LRRK2 G2019S astrocytes (Figure 1E-F).
36 Both LRRK2 G2019S MVBs and secreted EVs were smaller than their WT counterparts (Figure
37 2 and 3E), and the mutant CD63⁺ MVBs lost their perinuclear distribution (Figure 5). We did not
38 observe a difference in the number of secreted CD63⁺ EVs between WT and LRRK2 G2019S
39 astrocytes (Figure 3C), suggesting that the secretion of at least one population of EVs is
40 independent of the astrocyte genotype. However, we cannot rule out that sub-populations of
41 CD63⁻ EVs may be differentially secreted in mutant astrocytes.

1 Accumulating evidence supports a role for LRRK2 in vesicular membrane-related pathways,
2 which could be mediated by the kinase activity of LRRK2 and the resulting phosphorylation of a
3 subset of Rab GTPases (Alessi & Sammler, 2018; Steger et al., 2016). Rab GTPases are
4 master regulators of vesicle biogenesis, and coordinate intracellular trafficking of vesicular
5 organelles including autophagosomes, lysosomes and MVBs (Alessi & Sammler, 2018). The
6 LRRK2 mutation G2019S results in a gain-of-function phenotype with increased kinase activity
7 and increased phosphorylation of Rab substrates (Steger et al., 2016). Thus, the observation
8 that the distribution and phenotype of MVBs and EVs is altered by LRRK2 G2019S (Figures 2
9 and 3) may correlate with dysregulation of Rab GTPase signaling cascades. In fact, genetic
10 manipulations of Rab27b in HeLa cells altered the size and distribution of CD63⁺ MVBs, but did
11 not change the size or protein content of the secreted EVs (Ostrowski et al., 2010). This
12 suggests that while Rab27b may mediate LRRK2 G2019S-related alterations in MVB phenotype
13 in astrocytes, it is likely that additional pathways are affected and alter EV morphology and
14 cargo loading. For example, future studies could elucidate whether the increased kinase activity
15 resulting from the LRRK2 G2019S mutation prevents EV maturation, as well as the rate of
16 astrocyte-derived EV production and release.

17 We found that two important PD-related proteins, LRRK2 and α Syn, were localized inside MVBs
18 and secreted in astrocyte-derived EVs (Figure 4 and 6, Supplementary Figure 3). Furthermore,
19 the LRRK2 G2019S mutation in astrocytes induced the accumulation of LRRK2 (Figure 4C-D)
20 and p- α Syn (Figure 6A-B) within MVBs. We observed a trend towards greater levels of LRRK2
21 in mutant EVs compared to WT, but no genotype-dependent changes in α Syn levels
22 (Supplementary Figure 3). However, the accumulation of p- α Syn in LRRK2 G2019S MVBs
23 suggests that this aggregation-prone form of α Syn may also accumulate in mutant EVs, and is
24 consistent with studies showing that cerebral levels of p- α Syn are elevated in LRRK2 G2019S
25 rodents (Longo et al., 2017). Furthermore, the LRRK2 mutation G2019S increases LRRK2
26 autophosphorylation at serine 1292 (pS1292), and pS1292-LRRK2 was found in higher levels in
27 EVs isolated from PD patients compared to healthy controls (Fraser, Moehle, Alcalay, West, &
28 Consortium, 2016; Wang et al., 2017). Further studies are needed to determine if pS1292-
29 LRRK2 and p- α Syn differentially accumulate in EVs secreted from LRRK2 G2019S vs WT
30 astrocytes, as differences in EV profile between EV derived from healthy or PD astrocytes could
31 open new avenues in the field of biomarker research. The investigation of biofluid-isolated EVs
32 as non-invasive disease diagnostic tools in PD is an emerging field (Thompson et al., 2016),
33 and the search for sensitive biomarkers is facing challenges. Many cell types, including cells of
34 the CNS (Fiandaca, Kapogiannis et al., 2015, Shi, Liu et al., 2014) but also non-disease-
35 relevant cell types, contribute to the pool of EVs isolated from biofluids. As a result, EV sub-
36 populations that would best serve as markers of the disease are diluted in the total pool of EVs,
37 which limits the sensitivity of a biomarker assay. Given the dysregulation of the EV secretory
38 pathway in LRRK2 G2019S astrocytes, we speculate that astrocyte-derived EVs form a sub-
39 population of interest that could provide a sensitive measure of disease progression. Astrocyte-
40 derived exosomes could be isolated based on their expression of the Glial Fibrillary Acidic
41 Protein (GFAP) or Glutamine Aspartate Transporter (GLAST) astrocyte markers (Venturini et
42 al., 2019; Willis et al., 2017; Winston et al., 2019), and their cargoes compared between healthy
43 donors and PD patients.

1

2 **Significance of EV trophic support in Parkinson's disease**

3 We also show that dopaminergic neurons internalize EVs secreted by WT or LRRK2 G2019S
4 astrocytes (Figure 7). For this investigation, we focused our observations on a well-defined sub-
5 population of EVs that can be genetically labeled with GFP, thus enabling the documentation of
6 their internalization in live neurons. The EV genotype did not affect the amount of CD63-GFP
7 exosomes taken up by dopaminergic neurons (Figure 7C), but LRRK2 G2019S exosomes
8 accumulated to greater levels in the neurites compared to the somas (Figure 7E). Our
9 observations suggest that the localization of internalized EVs can vary based on the genotype of
10 the donor astrocyte. However, the functional consequences of EV localization in the recipient
11 neurons are unclear. Studies found that the composition of EVs and the health status of donor
12 and recipient cells can affect EV secretion and uptake (French, Antonyak, & Cerione, 2017),
13 and could therefore alter astrocyte-to-neuron EV-mediated communication. Our study identified
14 the PD-related proteins LRRK2 and α Syn in EV-enriched fractions (Supplementary Figure 3),
15 but their effect in the recipient neurons is unknown. Further studies including proteomics-based
16 characterization of WT and LRRK2 G2019S astrocyte-derived EVs are needed to more
17 thoroughly determine their composition, and which relevant cargoes (or lack of) affect the
18 physiology of the recipient neurons.

19 In support of our observations suggesting the dysregulation of EV-related pathways in LRRK2
20 G2019S astrocytes, we found that conditioned medium and EV-enriched fractions prepared
21 from mutant astrocytes failed to provide neurotrophic support compared to WT astrocytes
22 (Figures 8 and 9). We showed that in presence of LRRK2 G2019S ACM or EVs, dopaminergic
23 neurons were not able to maintain their neurite length, as observed by a shortening of the
24 neurites equivalent to that of neurons cultured in absence of trophic factors. However, we did
25 not observe excessive neurite shortening (≤ 50 % WT length) or fragmentation indicative of the
26 presence of toxic factors (di Domenico et al., 2019; Liddelow et al., 2017). A previous study
27 proposed a neurotoxic effect of LRRK2 G2019S astrocytes on dopaminergic neurons, possibly
28 mediated by the transfer and accumulation of astrocytic α Syn in neurons (di Domenico et al.,
29 2019). While the proposed mechanisms of LRRK2 G2019S astrocyte-mediated effect on
30 dopaminergic neurons appear to differ in the two studies, they are not mutually exclusive, and
31 astrocytes could secrete neurotoxic molecules as well as fail to secrete EV-enclosed
32 neurotrophic factors. In conclusion, our study suggests a novel effect of the PD-related mutation
33 LRRK2 G2019S in astrocytes, and in their ability to support dopaminergic neurons. This study
34 supports a model of astrocyte-to-neuron signaling and trophic support mediated by EVs, and
35 dysregulation of this pathway contributes to LRRK2 G2019S astrocyte-mediated dopaminergic
36 neuron atrophy.

37

38

1 Materials and Methods

2 Key resources table

Reagent type (species) or resource	Designation	Source or reference	Identifiers	Additional information
Antibody	Alexa Fluor-conjugated secondary antibodies	Thermo Fisher Scientific	Multiple	IF 1:1000
Antibody	anti-alpha-synuclein (rabbit monoclonal)	Abcam	ab138501	IF 1:200
Antibody	anti-APC magnetic beads	Miltenyi	130-090-855	MACS 1:5
Antibody	anti-CD133, APC-conjugated (mouse monoclonal)	BD Biosciences	566596	MACS 1:20
Antibody	anti-CD44 (rat monoclonal)	BD Biosciences	550538	IF 1:500
Antibody	anti-CD63 (mouse monoclonal)	Thermo Fisher Scientific	MA1-19281	IF 1:500. IEM: 1:40
Antibody	anti-GFAP (mouse monoclonal)	BD Biosciences	556328	IF 1:500
Antibody	anti-LRRK2 (rabbit monoclonal)	Abcam	ab133474	IF 1:200. IEM 1:20
Antibody	anti-MAP2 (chicken polyclonal)	Thermo Fisher Scientific	PA1-10005	IF 1:3000
Antibody	anti-mouse IgG conjugated to 12-nm gold particles (goat polyclonal)	Jackson ImmunoResearch	115-205-146	IEM 1:20
Antibody	anti-mouse IgG conjugated to 6-nm gold particles (goat polyclonal)	Jackson ImmunoResearch	115-195-146	IEM 1:40
Antibody	anti-phospho alpha-synuclein (S129) (rabbit monoclonal)	Abcam	ab51253	IEM 1:20
Antibody	anti-rabbit IgG conjugated to 6-nm gold particles (goat polyclonal)	Jackson ImmunoResearch	111-195-144	IEM 1:40
Antibody	anti-TH (rabbit polyclonal)	PhosphoSolutions	2025-THRAB	IF 1:500
Antibody	anti-vimentin (rat monoclonal)	R&D	MAB2105	IF 1:100
Cell line (<i>Homo sapiens</i>)	Human midbrain astrocytes	ScienCell	1850	
Cell line (<i>Homo sapiens</i>)	Isogenic control iPSCs	(Reinhardt et al., 2013)	IM2-GC	Prof. Dr. Thomas Gasser (Universitätsklinikum Tübingen) and Prof. Dr. Hans R. Schöler (Max-Planck Institute)
Cell line (<i>Homo sapiens</i>)	LRRK2 G2019S iPSCs	(Reinhardt et al., 2013)	IM2	Prof. Dr. Thomas Gasser (Universitätsklinikum Tübingen) and Prof. Dr. Hans R. Schöler (Max-Planck Institute)

Chemical compound, drug	Ascorbic acid	Sigma	A92902	
Chemical compound, drug	CHIR99021	Stemcell Technologies	72054	
Chemical compound, drug	Cytosine β -D-arabinofuranoside (AraC)	Sigma	C1768	
Chemical compound, drug	DAPT	Tocris Bioscience	2634	
Chemical compound, drug	dibutyryl cAMP	Millipore Sigma	28745	
Chemical compound, drug	LDN193189 hydrochloride	Sigma	SML0559	
Chemical compound, drug	Purmorphamine	Millipore Sigma	540223	
Chemical compound, drug	ROCK inhibitor (Y-27632)	Stemcell Technologies	72304	
Chemical compound, drug	SB431542	Stemcell Technologies	72234	
Commercial assay or kit	Control library phiX	Illumina	FC-110-3001	
Commercial assay or kit	ExoELISA-ULTRA Complete Kit (CD63 Detection)	System biosciences	EXEL-ULTRA-CD63-1	
Commercial assay or kit	KAPA library quantification kit	Roche	7960298001	
Commercial assay or kit	KAPA SYBR FAST qPCR kit	Roche	7959397001	
Commercial assay or kit	Nextera XT DNA library preparation kit	Illumina	FC-131-1024	
Commercial assay or kit	RevertAid First Strand cDNA Synthesis Kit	Thermo Fisher Scientific	K1622	
Commercial assay or kit	RNA purification kit	Qiagen	74104	
Commercial assay or kit	Taqman LRRK2 SNP genotyping assay	Thermo Fisher Scientific	4351379	
Other	96-well plates with optically clear bottom	Ibidi	89626	
Other	LD columns	Miltenyi Biotech	130-042-901	
Other	Polycarbonate aluminum bottles with cap assembly	Beckman Coulter	355618	
Other	Prolong Diamond with DAPI	Thermo Fisher Scientific	P36962	
Peptide, recombinant protein	BDNF (recombinant human)	PeproTech	450-02	
Peptide, recombinant protein	EGF (recombinant human)	Thermo Fisher Scientific	PHG0311	
Peptide, recombinant protein	FGF basic (146 aa) (recombinant human)	R&D Systems	233-FB-025	

Peptide, recombinant protein	GDNF (recombinant human)	PeproTech	450-10	
Peptide, recombinant protein	SHH(C25II) (recombinant mouse)	R&D Systems	464-SH-200	
Peptide, recombinant protein	TGF- β 3 (recombinant human)	R&D Systems	8420-B3-025	
Recombinant DNA reagent	pCT-CD63-GFP	System Biosciences	CYTO120-PA-1	
Sequence-based reagent	Human CD82_F	This paper	qPCR primer	⁵ GGTTTCGT GGAAGGAAG C ³
Sequence-based reagent	Human CD82_R	This paper	qPCR primer	⁵ AAGATCAA GTTGAAGAG GAAGAG ³
Sequence-based reagent	Human Rab27b_F	This paper	qPCR primer	⁵ AACTGGAT GAGCCTCACT G ³
Sequence-based reagent	Human Rab27b_R	This paper	qPCR primer	⁵ CTTGCCGT TCATTGACT TC ³
Software, algorithm	Beacon Designer Lite 8.16	Premier Biosoft (San Francisco, CA)	N/A	
Software, algorithm	Database for Annotation, Visualization and Integrated Discovery (DAVID) v6.8	N/A	https://david.ncicrf.gov	
Software, algorithm	EBseq v3.8	(Leng et al., 2013)	http://www.bioconductor.org/packages/devel/bioc/html/EBSeq.html	
Software, algorithm	ComplexHeatmap v3.11	(Z. Gu, Eils, & Schlesner, 2016)	http://bioconductor.org/packages/release/bioc/html/ComplexHeatmap.html	
Software, algorithm	Imaris 9.3	Bitplane (Belfast, UK)	N/A	
Software, algorithm	STAR v.2.7.3a	(Dobin et al., 2013)	https://github.com/alexdobin/STAR/releases	
Software, algorithm	Starcode v1.1	(Zorita, Cusco, & Filion, 2015)	https://github.com/gui11aume/starcode	

1

2 **Culture of iPSCs**

3 Patient-derived iPSCs with the LRRK2 mutation G2019S and the corresponding isogenic control
4 were provided by Prof. Dr. Thomas Gasser (Universitätsklinikum Tübingen) and Prof. Dr. Hans
5 R. Schöler (Max-Planck Institute). The cells were genotyped to confirm the presence of the
6 LRRK2 mutation G2019S using a TaqMan SNP genotyping assay (Thermo Fisher Scientific,
7 Waltham, MA), and karyotyped every 2 months to confirm genomic stability (Cell Line Genetics,
8 Madison, WI). The iPSCs were cultured in mTesR1 or mTesR Plus medium (StemCell
9 Technologies, Vancouver, Canada), regularly passaged as aggregates using ReLeSR
10 (StemCell Technologies), and cultured on Geltrex-coated plates (Thermo Fisher Scientific).

11

1 ***Preparation and culture of iPSC-derived NPCs, dopaminergic neurons and astrocytes***

2 The step-by-step protocols, media recipes and quality control experiments to prepare iPSC-
3 derived NPCs, dopaminergic neurons and astrocytes have been described in extensive detail
4 (de Rus Jacquet, 2019). Briefly, iPSCs were plated at a density of 1.6×10^6 cells/well of a
5 Geltrex-coated 6-well plate, and neuralized by dual SMAD inhibition (Kriks et al., 2011): day 0
6 (100 nM LDN193189, 10 μ M SB431542), day 1 and 2 (100 nM LDN193189, 10 μ M SB431542,
7 SHH 100 ng/mL, purmorphamine 2 μ M), day 3 and 5 (100 nM LDN193189, 10 μ M SB431542,
8 100 ng/mL SHH, 2 μ M purmorphamine, 3 μ M CHIR99021), day 7 and 9 (100 nM LDN193189, 3
9 μ M CHIR99021). At day 11, the cells were harvested and replated at 7×10^6 cells/well on a
10 Geltrex-coated 6-well plate. At day 11 and day 12, the medium was supplemented with 3 μ M
11 CHIR99021, 20 ng/mL FGF2 and 20 ng/mL EGF. At day 13, the differentiation of the iPSCs into
12 midbrain floor-plate NPCs was complete, and the cells were maintained in NPC medium
13 (NB/B27, 20 ng/mL FGF2 and 20 ng/mL EGF) supplemented with ROCK inhibitor (Y-27632,
14 Stemcell Technologies) at each single-cell passage.

15 To prepare dopaminergic neurons, NPCs were harvested in Accumax cell dissociation solution
16 (Innovative Cell Technologies, San Diego, CA) and plated at 7×10^6 cells/well on a Geltrex-
17 coated 6-well plate. The next day, NPCs were washed with DPBS and incubated in neuron
18 differentiation medium (NB/B27, 0.5 mM dibutyryl cAMP, 10 μ M DAPT, 0.2 mM ascorbic acid,
19 20 ng/mL BDNF, 20 ng/mL GDNF, 1 ng/mL TGF- β 3) (Kriks et al., 2011). Neuron differentiation
20 medium was replaced every 2 days for a total of 7 to 10 days. The resulting culture consisted of
21 neurons and undifferentiated NPCs. To isolate a pure neuronal population, the cells were
22 harvested in Accumax medium, diluted to a density of 1×10^6 cells in 100 μ l MACS buffer
23 (HBSS, 1 % v/v sodium pyruvate, 1 % GlutaMAX, 100 U/ml penicillin/streptomycin, 1 % HEPES,
24 0.5 % bovine serum albumin) supplemented with CD133 antibody (5 % v/v, BD Biosciences,
25 San Jose, CA, cat. # 566596), and the CD133⁺ NPCs were depleted by magnetic-activated cell
26 sorting (MACS) using an LD depletion column (Miltenyi Biotech, San Diego, CA), as described
27 previously (de Rus Jacquet, 2019).

28 To prepare astrocytes, NPCs were plated on Geltrex-coated plates at 15,000 cells/cm² in
29 ScienCell astrocyte medium (ScienCell Research Laboratories, Carlsbad, CA), passaged every
30 7 days at 15,000 cells/cm², and cryopreserved after 28 days of differentiation or used for
31 experiments (de Rus Jacquet, 2019; Tcw et al., 2017).

32

33 ***Culture of primary human astrocytes***

34 Fetal human midbrain astrocytes were obtained from ScienCell Research Laboratories. To
35 match the gender of the iPSCs used in this study, the primary astrocytes were selected from a
36 female donor. The cells were cultured in Astrocyte Medium (ScienCell Research Laboratories),
37 plated at a density of 40,000 cells/cm², cultured for 48 h, and harvested in TRIzol for RNA-seq
38 analysis.

39

40

1 ***Isolation of extracellular vesicles and preparation of EV-free ACM***

2 EVs were isolated from ACM by ultracentrifugation following an established protocol
3 (Purushothaman, 2019). Astrocytes were plated in ScienCell astrocyte medium, at a density of
4 40,000 cells/cm² in 15 cm dishes (5 to 8 dishes depending on the number of astrocytes
5 available), and grown to confluence for 24 h. The cells were subsequently triple washed with
6 PBS to remove cell debris and traces of FBS, and 25 mL of NB/B27 medium was added to each
7 15 cm dish. The ACM was collected twice, at 48 h intervals, and processed for EV isolation at
8 4°C. First, large debris was removed by serial centrifugation steps in a Sorvall ST8R centrifuge
9 (Thermo Fisher Scientific) at 300 x g for 10 min and at 2,000 x g for 20 min, followed by 12,000
10 rpm for 30 min using a fixed angle type 70 Ti rotor (Beckman Coulter, Brea, CA) and
11 polycarbonate aluminum bottles with cap assembly (Beckman Coulter). The cleared
12 supernatant was subsequently centrifuged at 40,000 rpm for 70 min to pellet the EVs using the
13 type 70 Ti rotor in an Optima XPN-80 ultracentrifuge (Beckman Coulter). The supernatant
14 resulting from this high-speed centrifugation is the EV-free ACM, and it was filtered through a
15 0.22 µm membrane and stored at -80°C. The EV pellet was resuspended in PBS and
16 centrifuged at 40,000 rpm for 70 min using the type 70 Ti rotor in an Optima XPN-80
17 ultracentrifuge (Beckman Coulter). The pellet obtained after this last centrifugation step was the
18 purified EV fraction, which was resuspended in PBS and processed immediately for cryo-EM or
19 aliquoted and stored at -80°C. The number of EVs collected in the EV-enriched fractions were
20 estimated by ELISA (System Biosciences). The ELISA standards provided in the kit are
21 calibrated by nanoparticle tracking analysis to measure the number of exosomes and establish
22 a standard curve based on exosome abundance, and therefore enable an estimation of the
23 number of exosomes in the experimental sample (Figure 3C).

24

25 ***Cryo-electron microscopy***

26 Cryo grids were prepared using two types of TEM grids: 400 mesh Quantifoil R1.2/1.3 grids with
27 empty holes and 400 mesh Quantifoil R1.2/1.3 grids coated with a 2 nm thin carbon layer
28 (Quantifoil Micro Tools GmbH, Germany). The grids were rendered hydrophilic by glow
29 discharge using a Pelco easiGlow glow discharger (Ted Pella Inc., CA) for 60 seconds, with a
30 current of 15 mA and a vacuum of 0.39 mbar. The cryo grids were then prepared using a Mark
31 IV Vitrobot (FEI Company, OR) with the operation chamber cooled to 4°C at a set humidity level
32 of 100 %. A total of 3 µl of fresh EVs was applied to a glow discharged grid. The grid was
33 subsequently blotted for 3 seconds from both sides with blot force 3, and plunged into a liquid
34 ethane bath for vitrification.

35 The cryo grids were loaded into a Tecnai F20 transmission electron microscope (FEI Company,
36 OR) for imaging through a side entry Gatan 626 cryo holder (Gatan Inc., CA). The microscope
37 was operated at 200 kV and was equipped with a standard Field Emission Gun (s-FEG) and a
38 Gatan K2 Summit direct electron detector (Gatan Inc., CA). Data collection was carried out
39 using the automation software package SerialEM (University of Colorado). To identify the
40 localization of the EVs on the grid, survey maps were first taken for various grid squares at a
41 nominal magnification of 1700x, with a calibrated pixel size of 2.15 nm (corresponding to a

1 calibrated magnification of 2325.6x). Once the EVs were identified on the survey maps, high
2 magnification images were taken at a nominal magnification of 29000x with a pixel size of 0.15
3 nm (corresponding to a calibrated magnification of 33333x). The illumination was set to produce
4 a dose rate of 10.5 electrons per pixel per second, and the K2 camera was operated in counted
5 mode with dose fractionation of 8 seconds total exposure time for 40 frames (0.2 seconds per
6 frame). Frames were aligned for motion correction using the default algorithm in SerialEM.

7

8 ***Transmission electron microscopy***

9 WT and LRRK2 G2019S astrocytes were cultured in 60 mm dishes to 80% confluence and
10 immersion fixed in freshly prepared 2% (w/v) paraformaldehyde (Sigma-Aldrich) and 2%
11 glutaraldehyde (Electron Microscopy Sciences, Hatfield, PA) in Hanks' balanced salt solution
12 (20 mM HEPES, pH 7.4) for 2 h at room temperature. To facilitate handling, cells were pelleted
13 and resuspended in 2 % (w/v) agar as described before (Paez-Segala et al., 2015). Cell pellets
14 were then post-fixed in 1% osmium tetroxide (Electron Microscopy Sciences, Hatfield, PA) for 1
15 h at room temperature, dehydrated in graded ethanol solutions (30%, 50%, 70%, 80%, 95%,
16 and 100%), and embedded in Eponate-12 (Ted Pella, Redding, CA). Ultrathin sections (60 nm)
17 were cut using a Leica UC6 ultramicrotomes, placed on Formvar/carbon-coated copper grids,
18 and stained with 3% aqueous uranyl acetate (15 minutes) and Sato's lead solution (5 minutes).
19 Sections were imaged using a FEI Spirit BioTWIN transmission electron microscope operating
20 at 80 kV, equipped with a 4k x 4k Gatan OneView Camera.

21

22 ***Immunogold electron microscopy***

23 Cultured astrocytes were fixed in 4% paraformaldehyde and 0.2% glutaraldehyde in Hanks'
24 balanced salt solution (20 mM HEPES, pH 7.4) for 2 h at room temperature. After pelleting,
25 samples were transferred to carriers filled with 20% BSA and frozen in a HPF Compact 01 high
26 pressure-freezing machine (M. Wohlwend GmbH, Sennwald, Switzerland) for cryo-
27 immobilization. Samples were freeze substituted in acetone containing 0.1% uranyl acetate plus
28 3% distilled water in a freeze substitution unit (Leica EM AFS2, Leica Microsystems, Buffalo
29 Grove, IL) at -90°C for 20 hours. Afterwards, the temperature was brought up slowly to -45°C ;
30 samples were rinsed with pure acetone, and infiltrated with 30%, 50%, and 70% Lowicryl HM20
31 resin (Polysciences Inc., Warrington, PA) in acetone for 2 h each followed by 100% HM20 resin
32 overnight. Samples were embedded in Lowicryl HM20 and UV polymerized for 2 days at -45°C
33 and 2 days at 20°C . Postembedding immunogold labeling was performed on ultrathin HM20
34 sections (70 nm) of astrocytes to detect CD63. The ultrathin sections were conditioned in
35 blocking buffer containing 1% BSA (w/v, Sigma-Aldrich), 0.01% (v/v) Triton X-100, and 0.01%
36 (v/v) Tween 20 in PBS for 20 min at room temperature, and incubated overnight at 4°C with an
37 anti-CD63 primary antibody (1:20 dilution, Thermo Fisher Scientific, cat. # MA1-19281) in
38 blocking buffer. After extensive rinses in PBS, sections were incubated for 2 h at room
39 temperature with a secondary antibody conjugated to 6-nm gold particles (Jackson
40 ImmunoResearch, cat # 115-195-146) diluted to 1:40 in blocking buffer. Samples were rinsed in
41 PBS, and then fixed with 1% (v/v) glutaraldehyde in PBS for 10 min. Gold particles were

1 amplified with silver enhancement (HQ silver kit from Nanoprobes, Yaphank, NY) for 4 min at
2 room temperature and contrast stained with 3% UA and Sato's triple lead.

3 For double-labeling experiments, cultured cells were fixed in 4% paraformaldehyde and 0.2%
4 glutaraldehyde in Hanks' balanced salt solution (20 mM HEPES, pH 7.4) for 2 h at room
5 temperature, pelleted in 2% (w/v) agar, cut into small blocks, and infused in 2 M sucrose
6 containing 15% (w/v) polyvinylpyrrolidone (10 kDa) for freezing. Samples were frozen and
7 ultrathin sections were prepared using a Leica UC6 ultramicrotome equipped with a Leica EM
8 FC6 cryochamber. The cryo-sections were lifted onto nickel grids and stored overnight on
9 gelatin at 4°C. Before immunolabeling, the gelatin was liquefied at 37°C, and the sections were
10 washed by floating the sections on droplets of PBS. For immunogold localization, the grids with
11 the attached thin sections were conditioned on droplets containing 1% (w/v) BSA, 0.01% (v/v)
12 Triton X-100, and 0.01% (v/v) Tween 20 in PBS (blocking buffer) for 10 min at room
13 temperature. Grids were incubated for 2 h in the presence of anti-LRRK2 (1:20 dilution, Abcam,
14 cat. # ab133474) and anti-CD63 antibodies (1:40 dilution), or anti-p- α Syn antibody (1:20
15 dilution, Abcam, cat. # ab51253) with mouse monoclonal anti-CD63 (1:40 dilution) in blocking
16 buffer. After extensive rinses in PBS, the sections were incubated for 1 h at 35°C with a
17 secondary antibody conjugated to 6-nm gold particles (1:40 dilution, Jackson ImmunoResearch,
18 cat # 111-195-144) and a secondary antibody conjugated to 12-nm gold particles (1:20 dilution,
19 Jackson ImmunoResearch, cat # 115-205-146) in blocking buffer. Lastly, grids with the attached
20 thin sections were rinsed in PBS, fixed with 2% (v/v) glutaraldehyde in PBS for 10 min, and
21 negative or positive contrast stained. Electron micrographs were taken with a FEI Spirit
22 BioTWIN transmission electron microscope operating at 80 kV, equipped with a 4k x 4k Gatan
23 OneView camera.

24

25 ***Immunofluorescence***

26 Cells were grown on German glass coverslips (Electron Microscopy Sciences) or 96-well plates
27 with an optically clear bottom (Ibidi, Gräfelfing, Germany) coated with Geltrex. The cells were
28 washed once with PBS and fixed by adding 4 % paraformaldehyde (Fisher Scientific, Waltham,
29 MA) for 20 minutes at room temperature. The cells were subsequently washed once with PBS,
30 and blocked/permeabilized in blocking buffer (0.3 % TX-100, 1 % BSA, 10 % FBS in PBS) for
31 one hour at room temperature. The cells were then washed once with PBS and incubated in
32 primary antibody overnight at 4°C with the following antibodies: anti-MAP2 (1:3000, Thermo
33 Fisher Scientific cat. # PA1-10005), TH (1:500, PhosphoSolutions, Aurora, CO, cat. # 2025-
34 THRAB), anti-CD63 (1:500, Thermo fisher Scientific cat. # MA1-19281), anti-LRRK2 (1:200,
35 Abcam cat. # ab133474), anti-GFAP (1:500, BD Biosciences, cat. # 556328), anti-vimentin
36 (1:100, R&D, Minneapolis, MN, cat. # MAB2105), and anti-CD44 (1:500, BD Biosciences, cat. #
37 550538) in BSA buffer (1 % BSA in PBS). The next day, the cells were washed twice with
38 DPBS, then incubated in Alexa-conjugated secondary antibodies (Thermo Fisher Scientific)
39 diluted 1:1000 in BSA buffer for 1 hour at room temperature. The cells were washed three times
40 with DPBS, then coverslips were mounted on slides with ProLong Diamond with DAPI (Thermo
41 Fisher Scientific) and cured for 24 h in the dark at room temperature.

1

2 **RNA isolation and RT-qPCR**

3 Confluent cell monolayers grown into individual wells of a Geltrex-coated 6-well plate were first
4 washed with DPBS to remove the cell culture medium and cell debris, then homogenized in
5 TRIzol (Thermo Fisher Scientific), and processed immediately or stored at -80°C. Chloroform
6 (20 % v/v) was added to the TRIzol samples, which were shaken vigorously for 20 seconds and
7 allowed to sit at room temperature for 3 min. The samples were subsequently centrifuged at
8 12,000 x g for 15 min, at 4°C, to separate the aqueous solution from the organic phase. The top,
9 aqueous phase was collected, and mixed 1:1 with ethanol. The RNA-containing samples were
10 processed using an RNeasy kit (Qiagen, Hilden, Germany, cat. #74104) following the
11 manufacturer's instructions, and the isolated RNA was processed immediately or stored at -
12 80°C. cDNA synthesis was carried out with a RevertAid First Strand cDNA Synthesis Kit
13 (Thermo Fisher Scientific) as described in the manufacturer's instructions. Forward and reverse
14 primers for RT-qPCR were designed at exon-exon junctions, using Beacon Designer Lite 8.16
15 (Premier Biosoft, San Francisco, CA). The primer sequences were as follows:

16 Human Rab27b: 5'AACTGGATGAGCCAAGT^{3'} (forward) and 5'CTTGCCGTTTCATTGACTTC^{3'}
17 (reverse)
18 Human CD82: 5'GGTTTCGTGGAAGGAAGC^{3'} (forward) and
19 5'AAGATCAAGTTGAAGAGGAAGAG^{3'} (reverse).

20 Each RT-qPCR measurement was performed in technical duplicates, with a total of four
21 independent biological replicates. Relative mRNA levels were calculated for each gene using
22 the formula:

$$23 \quad 2^{-\Delta\Delta Ct} = 2^{-\{(Ct, TG - Ct, \beta actin)_{LRRK2 G2019S} - (Ct, TG - Ct, \beta actin)_{WT}\}}$$

23

24 where "Ct, TG" represents the cycle threshold (Ct) for the target gene (TG), and "Ct, β actin"
25 represents the cycle threshold for the loading reference *Actb* (β -actin). The KAPA SYBR FAST
26 qPCR (Roche, Basel, Switzerland) master mix was used to prepare the reactions, and RT-
27 qPCR was performed using a Roche LightCycler 480.

28

29 **RNA-sequencing and analysis**

30 Samples were homogenized in TRIzol, then total RNA was isolated according to the
31 manufacturer's instructions, quantified by Nanodrop (Thermo Fisher Scientific), and diluted to 1
32 ng/ μ l in nuclease-free water. A total of 1 ng of RNA was added to 2.5 μ l of cell lysis buffer
33 (nuclease-free water with 0.2 % v/v Triton X-100 and 0.1 U/ μ l RNase inhibitor), and subjected to
34 cDNA synthesis and amplification as described before (Cembrowski et al., 2018). Libraries were
35 prepared using a modified Nextera XT DNA protocol (Illumina, San Diego, CA) where 5 μ M
36 P5NEXTPT5 was substituted for the i5 primers in the kit. Libraries were quantified by qPCR
37 (Roche), normalized to 2 nM, then pooled and sequenced on a NextSeq550 flowcell with 25

1 bases in read 1, 8 bases in the i7 index read, and 50 bases in read 2. The control library phiX
2 (Illumina) was spiked in at a final concentration of 15% to improve color balance in read 1.

3

4 *Smrtscrb2 analysis pipeline.*

5 Custom python scripts were used to extract Barcode and UMI sequences from read 1. The
6 correction of barcode error was achieved using starcode v1.1 (Zorita et al., 2015) with the
7 following additional parameters: “-d 1 -q --print_clusters”. Read 2 sequences were renamed
8 using the error-corrected barcode from starcode and UMI sequences from read 1, and were
9 aligned to the Homo sapiens GRCh38.p12 genome assembly and annotation from Ensembl
10 (ensembl.org) using STAR (Dobin et al., 2013) with the following additional parameters: “--
11 alignIntronMax 200000 --outSAMattributes All --outSAMunmapped Within --outSAMtype BAM
12 Unsorted”. The validity of an alignment was defined by the unique alignment to an exon feature
13 on the correct strand. Gene-level counts were created using valid alignments with at least 50%
14 of the read aligned to an exon feature, using a custom python script to collapse UMIs by gene.
15 All custom scripts are available by request.

16 Differential gene expression analysis was performed using EBseq v3.8 in R (Leng et al., 2013),
17 with condition 1 being LRRK2 G2019S and condition 2 being WT. EBseq calculated a median
18 normalization of the sequencing counts using the median of ratios methods (Anders & Huber,
19 2010). First, the geometric mean of the sequencing counts was calculated for each gene and
20 across all samples to create a pseudo-reference sample, and the ratio of the sequencing counts
21 to the pseudo-reference counts was calculated for every gene. Then, for each sample, the
22 median value of all the ratios was taken as the normalization factor. Finally, the median
23 normalized sequencing counts were calculated by dividing the sample’s sequencing counts by
24 the sample’s normalization factor. A false discovery rate of 0.05 and a fold change threshold of
25 1.4 or 0.7 were used to identify dysregulated genes in LRRK2 G2019S vs WT astrocytes. A k-
26 means clustering algorithm (k=3) was used to group genes into low, moderate and highly
27 expressed transcripts based on their $\log_{10}(1+\text{median normalized counts})$ value, using
28 ComplexHeatmap v3.11 in R (Z. Gu et al., 2016). Gene ontology enrichment analysis was done
29 using the Database for Annotation, Visualization, and Integrated Discovery (DAVID v6.8,
30 <https://david.ncifcrf.gov/>) (Huang da, Sherman, & Lempicki, 2009a, 2009b). A list of all genes
31 detected in all the samples was exported for use as the background gene set in DAVID.

32

33 ***Accession numbers***

34 Raw RNA-seq datasets have been deposited in the GEO data repository (NCBI), accession
35 number GSE152768.

36

37 ***Internalization of CD63⁺ exosomes by dopaminergic neurons***

38 The study of the internalization of astrocyte-derived EVs by dopaminergic neurons followed a
39 specific multi-step protocol that is detailed below: (1) prepare separate cultures of dopaminergic

1 neurons and astrocytes, (2) transduce each cell type to express a protein of interest (tdTomato
2 or CD63-GFP), (3) harvest the astrocytes and plate them directly on the neurons, and (4)
3 monitor the internalization of EVs by live cell microscopy. As a first step to this protocol,
4 astrocytes were plated at 40,000 cells/cm² in ScienCell astrocyte medium, and transduced the
5 next day with a lentivirus expressing CD63-GFP (produced from pCT-CD63-GFP, System
6 Biosciences, Palo Alto, CA). The astrocytes expressed GFP between 48 and 72 h after
7 transduction. In parallel, iPSC-derived dopaminergic neurons were plated at 70,000 cells/well in
8 a Geltrex-coated 96-well optically clear plate (Ibidi) in neuron differentiation medium. After 2 to 3
9 days in culture, the dopaminergic neurons were transduced with an adeno-associated virus rh10
10 vector expressing CAG-tdTomato. After 72 h, the rh10-CAG-tdTomato-containing medium was
11 removed, and 20,000 CD63-GFP astrocytes were plated in each neuron-containing well of the
12 96-well plate, on top of the tdTomato dopaminergic neurons. To ensure a healthy co-culture, the
13 cells were maintained in NB/B27 with 0.5 % FBS. At the time of imaging, the cell culture
14 medium was changed to pre-warmed phenol red-free medium to reduce nonspecific
15 background fluorescence. The uptake of astrocyte-secreted CD63-GFP EVs by dopaminergic
16 neurons was monitored by live-cell confocal microscopy, using a temperature and CO₂-
17 controlled incubation chamber mounted on a Zeiss LSM 880 inverted laser scanning confocal
18 microscope.

19

20 ***Confocal and widefield microscopy***

21 The following microscopes were used: (1) Zeiss LSM 880 inverted laser scanning confocal
22 microscope equipped with a plan-apochromatic 63x oil objective lens (Zeiss, NA = 1.4), 40x oil
23 objective lens (Zeiss, NA = 1.3), 405 nm, 488 nm and 561 nm laser lines, and ZEN software
24 (Zeiss, Oberkochen, Germany). (2) Nikon Eclipse TiE inverted microscope equipped with a CFI
25 Plan Apo Lambda 10x (Nikon Instruments, NA = 0.45) and a CFI Plan Apo VC 60x oil objective
26 lens (Nikon Instruments, NA = 1.4), sCMOS camera (Zyla 4.2, Andor), SPECTRA X light engine
27 illumination source (Lumencor, Beaverton, OR), and NIS-Elements software (Nikon Instruments,
28 Tokyo, Japan). The experimental details for each imaging experiment are provided in the
29 appropriate subsection in Materials and Methods.

30

31 ***Image analysis***

32 *CD63⁺ marker distribution in astrocytes.* Images in Zeiss CZI file format were properly converted
33 to Imaris native IMS file format, and analyzed in Imaris 9.3 (Bitplane, Belfast, UK). Each image
34 was composed of three channels representing the CD44 membrane marker, CD63
35 exosome/MVB marker, and DAPI nuclear marker. The components in each fluorescence
36 channel were detected using the cell creation wizard without the need for additional image
37 preprocessing. Intensity thresholds were calculated for each channel such that the values were
38 applied to all datasets since they were acquired using identical acquisition settings to minimize
39 user bias; however, for cases in which the cytoplasmic staining was heterogeneous, the
40 intensity thresholds were manually adjusted. For nucleus detection, a size filter was used to
41 remove small and irregular shapes. For cell detection, a surface was generated by expanding it

1 on a single nucleus accompanied by a size filter. For vesicle detection, CD63⁺ structures were
2 modeled as spots with an estimated diameter of 0.8 μm with region growing disabled. Statistics
3 were exported for each cell object, and “Vesicles Distance to Closest Nucleus” statistics were
4 used to analyze CD63⁺ MVB distribution in astrocytes.

5 *Colocalization of LRRK2 and CD63.* Images in Zeiss CZI file format were properly converted to
6 Imaris native IMS file format, and analyzed in Imaris 9.3. All fluorescence channels were first
7 deconvolved using the “robust” algorithm (15 iterations) in Imaris ClearView which estimated the
8 PSF based on a widefield fluorescence template and the acquisition parameters used. A
9 surface object was created for the CD63 (exosome/MVB) channel with background subtraction
10 enabled (Gaussian filter width of 1 μm). LRRK2 was detected as spots with an estimated
11 diameter of 0.4 μm and with background subtraction enabled; “region growing on spots” was
12 used to more accurately determine their intersections with surfaces. Once LRRK2 spots were
13 created, they were segregated into two populations depending on if the distances from the spot
14 centers to the exterior of CD63 surface objects were greater than 0.2 μm (half the estimated
15 diameter); this was accomplished using the “Find Spots Close To Surface” MATLAB
16 (Mathworks, Natick, MA) algorithm from Imaris XTensions. A cell object was then created by
17 importing CD63 surface objects as cells and LRRK2-associated spots as vesicles. The relevant
18 statistics for each LRRK2 spot, including the cell IDs corresponding to the associated CD63
19 surface objects, were exported. The data were aggregated in MATLAB to generate histograms.

20 *Internalization of CD63-GFP EVs by dopaminergic neurons.* Confocal z-stack images were
21 properly converted from Zeiss CZI file format to Imaris native IMS file format, and analyzed in
22 Imaris 9.3. The green channel with the CD63-GFP signal was first deconvolved (10 iterations) in
23 Imaris ClearView which estimated the PSF based on a confocal fluorescence template and the
24 acquisition parameters used. The red channel with the tdTomato signal was processed with a
25 Gaussian Filter (0.18 μm filter width) to reduce image noise. A total of three layers were created
26 to represent the total neuronal surfaces, soma-only surfaces and CD63-GFP EVs. Neuronal
27 surfaces encompassing the soma and neurites were modeled using the “surface” tool with
28 background subtraction and a sphericity filter to remove background signal. The soma layer was
29 modeled using the “surface” tool with background subtraction enabled, “split touching objects”
30 enabled, and with seed point diameters of 10 μm to eliminate non-soma surfaces. The resulting
31 surfaces created by Imaris were manually curated if necessary, to trim and delete non-soma
32 surfaces and ensure an accurate representation of the somas. CD63-GFP exosomes were
33 detected as spots with an estimated diameter of 0.4 μm and background subtraction enabled.
34 Once CD63 spots were created, they were segregated into two populations (intracellular and
35 extracellular) depending on their distances from the spot centers to the exterior of neuron or
36 soma surface objects; this was accomplished using the “Find Spots Close To Surface” MATLAB
37 (Mathworks, Natick, MA) algorithm from Imaris XTensions.

38 *Astrocyte effects on dopaminergic neurons viability and morphological changes.* Dopaminergic
39 neurons were identified as MAP2⁺/TH⁺ populations, and the number of MAP2⁺/TH⁺ neurons after
40 experimental treatments were counted as a measure of neuronal viability. The length of the
41 dendrites was measured by tracing the MAP2 signal of dopaminergic neurons using the NIS
42 Elements (Nikon Instruments) tracing tool. Sample identity was masked using a numerical code
43 to blind the experimenter during image analysis.

1

2 **Statistical analysis**

3 Data was analyzed using GraphPad Prism version 8.0 (La Jolla, CA). P-values were calculated
4 using two-tailed unpaired Student's t-test assuming equal standard deviation (Figures 1E, 1F,
5 2B, 3C, 3E, 4B, 7C, 7D, 8B-C, and 8E), Mann-Whitney test (Figure 5B), Chi-square test
6 (Figures 4D and 6B), or using one-way ANOVA with Newman-Keuls multiple comparisons
7 (Figure 7E) or Tukey's multiple comparisons correction (Figures 8E, 9A, and 9C).

8

9 **Acknowledgements**

10 The authors would like to thank members of the O'Shea lab, and our colleagues Dr. Deepika
11 Walpita, Dr. Jennifer Lippincott-Schwartz, Dr. Ulrike Heberlein, and Dr. Erik Snapp for helpful
12 discussions and feedback, and Michelle Quiambao for administrative support. We also thank Dr.
13 Damien Alcor and the Light Microscopy Center at Janelia for assistance setting up the imaging
14 platform, Dr. Zhiheng Yu and the staff at Janelia's Cryo-Electron Microscopy and Electron
15 Microscopy Center, and the staff at Janelia's Virus Services. We thank Prof. Dr. Thomas
16 Gasser (Universitätsklinikum Tübingen) and Prof. Dr. Hans R. Schöler (Max-Planck Institute) for
17 providing the iPSCs with the LRRK2 G2019S mutation and isogenic control. This work was
18 supported by the Howard Hughes Medical Institute.

19

20 **Competing interests**

21 Erin K O'Shea: President at the Howard Hughes Medical Institute, one of the three founding
22 funders of *eLife*.

23

24 **References**

- 25 Alessi, D. R., & Sammler, E. (2018). LRRK2 kinase in Parkinson's disease. *Science*, *360*(6384),
26 36-37. doi:10.1126/science.aar5683
- 27 Allen, N. J., & Eroglu, C. (2017). Cell Biology of Astrocyte-Synapse Interactions. *Neuron*, *96*(3),
28 697-708. doi:10.1016/j.neuron.2017.09.056
- 29 Allen, N. J., & Lyons, D. A. (2018). Glia as architects of central nervous system formation and
30 function. *Science*, *362*(6411), 181-185. doi:10.1126/science.aat0473
- 31 Anders, S., & Huber, W. (2010). Differential expression analysis for sequence count data.
32 *Genome Biol*, *11*(10), R106. doi:10.1186/gb-2010-11-10-r106
- 33 Andreu, Z., & Yanez-Mo, M. (2014). Tetraspanins in extracellular vesicle formation and function.
34 *Front Immunol*, *5*, 442. doi:10.3389/fimmu.2014.00442
- 35 Banker, G. A. (1980). Trophic interactions between astroglial cells and hippocampal neurons in
36 culture. *Science*, *209*(4458), 809-810. doi:10.1126/science.7403847
- 37 Basso, M., Pozzi, S., Tortarolo, M., Fiordaliso, F., Bisighini, C., Pasetto, L., . . . Bonetto, V.
38 (2013). Mutant copper-zinc superoxide dismutase (SOD1) induces protein secretion

- 1 pathway alterations and exosome release in astrocytes: implications for disease
2 spreading and motor neuron pathology in amyotrophic lateral sclerosis. *J Biol Chem*,
3 288(22), 15699-15711. doi:10.1074/jbc.M112.425066
- 4 Bonifati, V. (2006). Parkinson's disease: the LRRK2-G2019S mutation: opening a novel era in
5 Parkinson's disease genetics. *Eur J Hum Genet*, 14(10), 1061-1062.
6 doi:10.1038/sj.ejhg.5201695
- 7 Cembrowski, M. S., Phillips, M. G., DiLisio, S. F., Shields, B. C., Winnubst, J., Chandrashekar,
8 J., . . . Spruston, N. (2018). Dissociable Structural and Functional Hippocampal Outputs
9 via Distinct Subiculum Cell Classes. *Cell*, 173(5), 1280-1292 e1218.
10 doi:10.1016/j.cell.2018.03.031
- 11 Chaudhuri, A. D., Dastgheyb, R. M., Yoo, S. W., Trout, A., Talbot, C. C., Jr., Hao, H., . . .
12 Haughey, N. J. (2018). TNFalpha and IL-1beta modify the miRNA cargo of astrocyte
13 shed extracellular vesicles to regulate neurotrophic signaling in neurons. *Cell Death Dis*,
14 9(3), 363. doi:10.1038/s41419-018-0369-4
- 15 Chiasserini, D., van Weering, J. R., Piersma, S. R., Pham, T. V., Malekzadeh, A., Teunissen, C.
16 E., . . . Jimenez, C. R. (2014). Proteomic analysis of cerebrospinal fluid extracellular
17 vesicles: a comprehensive dataset. *J Proteomics*, 106, 191-204.
18 doi:10.1016/j.jprot.2014.04.028
- 19 Clarke, L. E., Liddelow, S. A., Chakraborty, C., Munch, A. E., Heiman, M., & Barres, B. A.
20 (2018). Normal aging induces A1-like astrocyte reactivity. *Proc Natl Acad Sci U S A*,
21 115(8), E1896-E1905. doi:10.1073/pnas.1800165115
- 22 Dawson, T. M., & Dawson, V. L. (2003). Molecular pathways of neurodegeneration in
23 Parkinson's disease. *Science*, 302(5646), 819-822. doi:10.1126/science.1087753
- 24 de Rus Jacquet, A. (2019). Preparation and Co-Culture of iPSC-Derived Dopaminergic Neurons
25 and Astrocytes. *Curr Protoc Cell Biol*, 85(1), e98. doi:10.1002/cpcb.98
- 26 Deemyad, T., Luthi, J., & Spruston, N. (2018). Astrocytes integrate and drive action potential
27 firing in inhibitory subnetworks. *Nat Commun*, 9(1), 4336. doi:10.1038/s41467-018-
28 06338-3
- 29 di Domenico, A., Carola, G., Calatayud, C., Pons-Espinal, M., Munoz, J. P., Richaud-Patin, Y., .
30 . . . Consiglio, A. (2019). Patient-Specific iPSC-Derived Astrocytes Contribute to Non-Cell-
31 Autonomous Neurodegeneration in Parkinson's Disease. *Stem Cell Reports*, 12(2), 213-
32 229. doi:10.1016/j.stemcr.2018.12.011
- 33 Di Giorgio, F. P., Boulting, G. L., Bobrowicz, S., & Egan, K. C. (2008). Human embryonic stem
34 cell-derived motor neurons are sensitive to the toxic effect of glial cells carrying an ALS-
35 causing mutation. *Cell Stem Cell*, 3(6), 637-648. doi:10.1016/j.stem.2008.09.017
- 36 Dobin, A., Davis, C. A., Schlesinger, F., Drenkow, J., Zaleski, C., Jha, S., . . . Gingeras, T. R.
37 (2013). STAR: ultrafast universal RNA-seq aligner. *Bioinformatics*, 29(1), 15-21.
38 doi:10.1093/bioinformatics/bts635
- 39 Escola, J. M., Kleijmeer, M. J., Stoorvogel, W., Griffith, J. M., Yoshie, O., & Geuze, H. J. (1998).
40 Selective enrichment of tetraspan proteins on the internal vesicles of multivesicular
41 endosomes and on exosomes secreted by human B-lymphocytes. *J Biol Chem*, 273(32),
42 20121-20127. doi:10.1074/jbc.273.32.20121

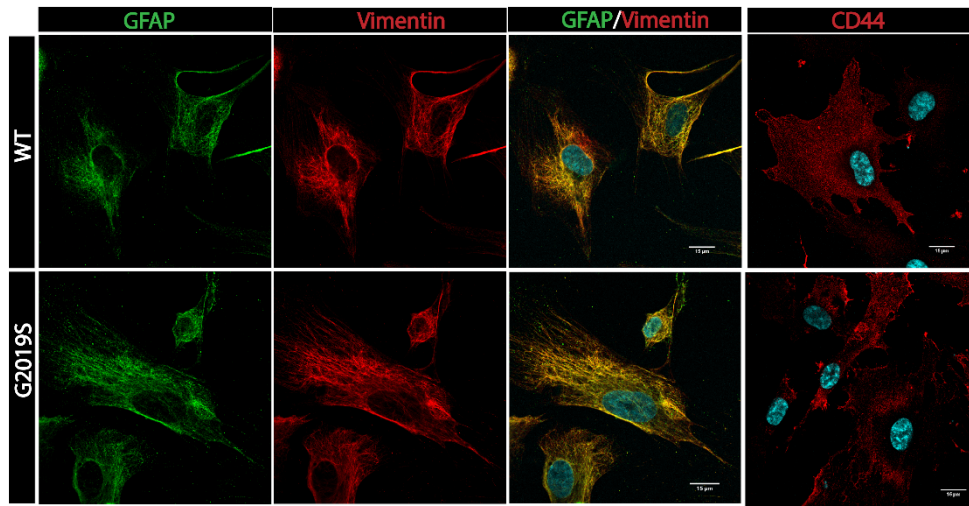
- 1 Fraser, K. B., Moehle, M. S., Alcalay, R. N., West, A. B., & Consortium, L. C. (2016). Urinary
2 LRRK2 phosphorylation predicts parkinsonian phenotypes in G2019S LRRK2 carriers.
3 *Neurology*, 86(11), 994-999. doi:10.1212/WNL.0000000000002436
- 4 Fraser, K. B., Rawlins, A. B., Clark, R. G., Alcalay, R. N., Standaert, D. G., Liu, N., . . . West, A.
5 B. (2016). Ser(P)-1292 LRRK2 in urinary exosomes is elevated in idiopathic Parkinson's
6 disease. *Mov Disord*, 31(10), 1543-1550. doi:10.1002/mds.26686
- 7 French, K. C., Antonyak, M. A., & Cerione, R. A. (2017). Extracellular vesicle docking at the
8 cellular port: Extracellular vesicle binding and uptake. *Semin Cell Dev Biol*, 67, 48-55.
9 doi:10.1016/j.semcdb.2017.01.002
- 10 Fujiwara, H., Hasegawa, M., Dohmae, N., Kawashima, A., Masliah, E., Goldberg, M. S., . . .
11 Iwatsubo, T. (2002). alpha-Synuclein is phosphorylated in synucleinopathy lesions. *Nat*
12 *Cell Biol*, 4(2), 160-164. doi:10.1038/ncb748
- 13 Gorbatyuk, O. S., Li, S., Sullivan, L. F., Chen, W., Kondrikova, G., Manfredsson, F. P., . . .
14 Muzyczka, N. (2008). The phosphorylation state of Ser-129 in human alpha-synuclein
15 determines neurodegeneration in a rat model of Parkinson disease. *Proc Natl Acad Sci*
16 *U S A*, 105(2), 763-768. doi:10.1073/pnas.0711053105
- 17 Gore, A., Li, Z., Fung, H. L., Young, J. E., Agarwal, S., Antosiewicz-Bourget, J., . . . Zhang, K.
18 (2011). Somatic coding mutations in human induced pluripotent stem cells. *Nature*,
19 471(7336), 63-67. doi:10.1038/nature09805
- 20 Gu, X. L., Long, C. X., Sun, L., Xie, C., Lin, X., & Cai, H. (2010). Astrocytic expression of
21 Parkinson's disease-related A53T alpha-synuclein causes neurodegeneration in mice.
22 *Mol Brain*, 3, 12. doi:10.1186/1756-6606-3-12
- 23 Gu, Z., Eils, R., & Schlesner, M. (2016). Complex heatmaps reveal patterns and correlations in
24 multidimensional genomic data. *Bioinformatics*, 32(18), 2847-2849.
25 doi:10.1093/bioinformatics/btw313
- 26 Haidet-Phillips, A. M., Hester, M. E., Miranda, C. J., Meyer, K., Braun, L., Frakes, A., . . .
27 Kaspar, B. K. (2011). Astrocytes from familial and sporadic ALS patients are toxic to
28 motor neurons. *Nat Biotechnol*, 29(9), 824-828. doi:10.1038/nbt.1957
- 29 Huang da, W., Sherman, B. T., & Lempicki, R. A. (2009a). Bioinformatics enrichment tools:
30 paths toward the comprehensive functional analysis of large gene lists. *Nucleic Acids*
31 *Res*, 37(1), 1-13. doi:10.1093/nar/gkn923
- 32 Huang da, W., Sherman, B. T., & Lempicki, R. A. (2009b). Systematic and integrative analysis
33 of large gene lists using DAVID bioinformatics resources. *Nat Protoc*, 4(1), 44-57.
34 doi:10.1038/nprot.2008.211
- 35 Ioannou, M. S., Jackson, J., Sheu, S. H., Chang, C. L., Weigel, A. V., Liu, H., . . . Liu, Z. (2019).
36 Neuron-Astrocyte Metabolic Coupling Protects against Activity-Induced Fatty Acid
37 Toxicity. *Cell*, 177(6), 1522-1535 e1514. doi:10.1016/j.cell.2019.04.001
- 38 Jorgensen, M., Baek, R., Pedersen, S., Sondergaard, E. K., Kristensen, S. R., & Varming, K.
39 (2013). Extracellular Vesicle (EV) Array: microarray capturing of exosomes and other
40 extracellular vesicles for multiplexed phenotyping. *J Extracell Vesicles*, 2.
41 doi:10.3402/jev.v2i0.20920
- 42 Kirkeby, A., Grealish, S., Wolf, D. A., Nelander, J., Wood, J., Lundblad, M., . . . Parmar, M.
43 (2012). Generation of regionally specified neural progenitors and functional neurons

- 1 from human embryonic stem cells under defined conditions. *Cell Rep*, 1(6), 703-714.
2 doi:10.1016/j.celrep.2012.04.009
- 3 Kriks, S., Shim, J. W., Piao, J., Ganat, Y. M., Wakeman, D. R., Xie, Z., . . . Studer, L. (2011).
4 Dopamine neurons derived from human ES cells efficiently engraft in animal models of
5 Parkinson's disease. *Nature*, 480(7378), 547-551. doi:10.1038/nature10648
- 6 Kumari, U., & Tan, E. K. (2009). LRRK2 in Parkinson's disease: genetic and clinical studies from
7 patients. *FEBS J*, 276(22), 6455-6463. doi:10.1111/j.1742-4658.2009.07344.x
- 8 Lamontagne-Proulx, J., St-Amour, I., Labib, R., Pilon, J., Denis, H. L., Cloutier, N., . . . Cicchetti,
9 F. (2019). Portrait of blood-derived extracellular vesicles in patients with Parkinson's
10 disease. *Neurobiol Dis*, 124, 163-175. doi:10.1016/j.nbd.2018.11.002
- 11 Leng, N., Dawson, J. A., Thomson, J. A., Ruotti, V., Rissman, A. I., Smits, B. M., . . .
12 Kendzierski, C. (2013). EBSeq: an empirical Bayes hierarchical model for inference in
13 RNA-seq experiments. *Bioinformatics*, 29(8), 1035-1043.
14 doi:10.1093/bioinformatics/btt087
- 15 Liddelow, S. A., & Barres, B. A. (2017). Reactive Astrocytes: Production, Function, and
16 Therapeutic Potential. *Immunity*, 46(6), 957-967. doi:10.1016/j.immuni.2017.06.006
- 17 Liddelow, S. A., Guttenplan, K. A., Clarke, L. E., Bennett, F. C., Bohlen, C. J., Schirmer, L., . . .
18 Barres, B. A. (2017). Neurotoxic reactive astrocytes are induced by activated microglia.
19 *Nature*, 541(7638), 481-487. doi:10.1038/nature21029
- 20 Longo, F., Mercatelli, D., Novello, S., Arcuri, L., Brugnoli, A., Vincenzi, F., . . . Morari, M. (2017).
21 Age-dependent dopamine transporter dysfunction and Serine129 phospho-alpha-
22 synuclein overload in G2019S LRRK2 mice. *Acta Neuropathol Commun*, 5(1), 22.
23 doi:10.1186/s40478-017-0426-8
- 24 Lynch-Day, M. A., Mao, K., Wang, K., Zhao, M., & Klionsky, D. J. (2012). The role of autophagy
25 in Parkinson's disease. *Cold Spring Harb Perspect Med*, 2(4), a009357.
26 doi:10.1101/cshperspect.a009357
- 27 Massano, J., & Bhatia, K. P. (2012). Clinical approach to Parkinson's disease: features,
28 diagnosis, and principles of management. *Cold Spring Harb Perspect Med*, 2(6),
29 a008870. doi:10.1101/cshperspect.a008870
- 30 a008870 [pii]
- 31 Men, Y., Yelick, J., Jin, S., Tian, Y., Chiang, M. S. R., Higashimori, H., . . . Yang, Y. (2019).
32 Exosome reporter mice reveal the involvement of exosomes in mediating neuron to
33 astroglia communication in the CNS. *Nat Commun*, 10(1), 4136. doi:10.1038/s41467-
34 019-11534-w
- 35 Ostrowski, M., Carmo, N. B., Krumeich, S., Fanget, I., Raposo, G., Savina, A., . . . Thery, C.
36 (2010). Rab27a and Rab27b control different steps of the exosome secretion pathway.
37 *Nat Cell Biol*, 12(1), 19-30; sup pp 11-13. doi:10.1038/ncb2000
- 38 Paez-Segala, M. G., Sun, M. G., Shtengel, G., Viswanathan, S., Baird, M. A., Macklin, J. J., . . .
39 Looger, L. L. (2015). Fixation-resistant photoactivatable fluorescent proteins for CLEM.
40 *Nat Methods*, 12(3), 215-218, 214 p following 218. doi:10.1038/nmeth.3225
- 41 Pascua-Maestro, R., Gonzalez, E., Lillo, C., Ganfornina, M. D., Falcon-Perez, J. M., & Sanchez,
42 D. (2018). Extracellular Vesicles Secreted by Astroglial Cells Transport Apolipoprotein D
43 to Neurons and Mediate Neuronal Survival Upon Oxidative Stress. *Front Cell Neurosci*,
44 12, 526. doi:10.3389/fncel.2018.00526

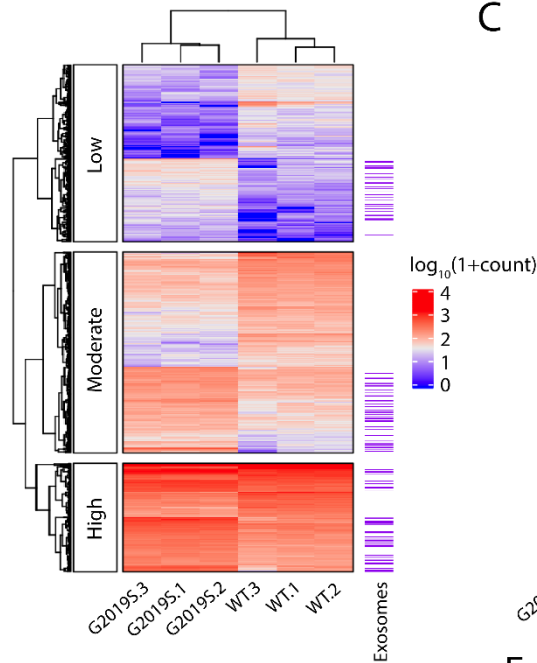
- 1 Pegtel, D. M., & Gould, S. J. (2019). Exosomes. *Annu Rev Biochem*, *88*, 487-514.
2 doi:10.1146/annurev-biochem-013118-111902
- 3 Purushothaman, A. (2019). Exosomes from Cell Culture-Conditioned Medium: Isolation by
4 Ultracentrifugation and Characterization. *Methods Mol Biol*, *1952*, 233-244.
5 doi:10.1007/978-1-4939-9133-4_19
- 6 Reinhardt, P., Schmid, B., Burbulla, L. F., Schondorf, D. C., Wagner, L., Glatza, M., . . .
7 Sternecker, J. (2013). Genetic correction of a LRRK2 mutation in human iPSCs links
8 parkinsonian neurodegeneration to ERK-dependent changes in gene expression. *Cell*
9 *Stem Cell*, *12*(3), 354-367. doi:10.1016/j.stem.2013.01.008
- 10 Shi, M., Liu, C., Cook, T. J., Bullock, K. M., Zhao, Y., Gingham, C., . . . Zhang, J. (2014). Plasma
11 exosomal alpha-synuclein is likely CNS-derived and increased in Parkinson's disease.
12 *Acta Neuropathol*, *128*(5), 639-650. doi:10.1007/s00401-014-1314-y
- 13 Soldner, F., Hockemeyer, D., Beard, C., Gao, Q., Bell, G. W., Cook, E. G., . . . Jaenisch, R.
14 (2009). Parkinson's disease patient-derived induced pluripotent stem cells free of viral
15 reprogramming factors. *Cell*, *136*(5), 964-977. doi:10.1016/j.cell.2009.02.013
- 16 Spampinato, S. F., Bortolotto, V., Canonico, P. L., Sortino, M. A., & Grilli, M. (2019). Astrocyte-
17 Derived Paracrine Signals: Relevance for Neurogenic Niche Regulation and Blood-Brain
18 Barrier Integrity. *Front Pharmacol*, *10*, 1346. doi:10.3389/fphar.2019.01346
- 19 Steger, M., Tonelli, F., Ito, G., Davies, P., Trost, M., Vetter, M., . . . Mann, M. (2016).
20 Phosphoproteomics reveals that Parkinson's disease kinase LRRK2 regulates a subset
21 of Rab GTPases. *Elife*, *5*. doi:10.7554/eLife.12813
- 22 Tcw, J., Wang, M., Pimenova, A. A., Bowles, K. R., Hartley, B. J., Lacin, E., . . . Brennand, K. J.
23 (2017). An Efficient Platform for Astrocyte Differentiation from Human Induced
24 Pluripotent Stem Cells. *Stem Cell Reports*, *9*(2), 600-614.
25 doi:10.1016/j.stemcr.2017.06.018
- 26 Temoche-Diaz, M. M., Shurtleff, M. J., Nottingham, R. M., Yao, J., Fadadu, R. P., Lambowitz, A.
27 M., & Schekman, R. (2019). Distinct mechanisms of microRNA sorting into cancer cell-
28 derived extracellular vesicle subtypes. *Elife*, *8*. doi:10.7554/eLife.47544
- 29 Thompson, A. G., Gray, E., Heman-Ackah, S. M., Mager, I., Talbot, K., Andaloussi, S. E., . . .
30 Turner, M. R. (2016). Extracellular vesicles in neurodegenerative disease - pathogenesis
31 to biomarkers. *Nat Rev Neurol*, *12*(6), 346-357. doi:10.1038/nrneuro.2016.68
- 32 Valenza, M., Marullo, M., Di Paolo, E., Cesana, E., Zuccato, C., Biella, G., & Cattaneo, E.
33 (2015). Disruption of astrocyte-neuron cholesterol cross talk affects neuronal function in
34 Huntington's disease. *Cell Death Differ*, *22*(4), 690-702. doi:10.1038/cdd.2014.162
- 35 Venturini, A., Passalacqua, M., Pelassa, S., Pastorino, F., Tedesco, M., Cortese, K., . . .
36 Cervetto, C. (2019). Exosomes From Astrocyte Processes: Signaling to Neurons. *Front*
37 *Pharmacol*, *10*, 1452. doi:10.3389/fphar.2019.01452
- 38 Wang, S., Liu, Z., Ye, T., Mabrouk, O. S., Maltbie, T., Aasly, J., & West, A. B. (2017). Elevated
39 LRRK2 autophosphorylation in brain-derived and peripheral exosomes in LRRK2
40 mutation carriers. *Acta Neuropathol Commun*, *5*(1), 86. doi:10.1186/s40478-017-0492-y
- 41 West, A. B., Moore, D. J., Biskup, S., Bugayenko, A., Smith, W. W., Ross, C. A., . . . Dawson, T.
42 M. (2005). Parkinson's disease-associated mutations in leucine-rich repeat kinase 2
43 augment kinase activity. *Proc Natl Acad Sci U S A*, *102*(46), 16842-16847.
44 doi:10.1073/pnas.0507360102

- 1 Willis, C. M., Menoret, A., Jellison, E. R., Nicaise, A. M., Vella, A. T., & Crocker, S. J. (2017). A
2 Refined Bead-Free Method to Identify Astrocytic Exosomes in Primary Glial Cultures and
3 Blood Plasma. *Front Neurosci*, *11*, 335. doi:10.3389/fnins.2017.00335
- 4 Winston, C. N., Romero, H. K., Ellisman, M., Nauss, S., Julovich, D. A., Conger, T., . . .
5 Rissman, R. A. (2019). Assessing Neuronal and Astrocyte Derived Exosomes From
6 Individuals With Mild Traumatic Brain Injury for Markers of Neurodegeneration and
7 Cytotoxic Activity. *Front Neurosci*, *13*, 1005. doi:10.3389/fnins.2019.01005
- 8 Yoshioka, Y., Konishi, Y., Kosaka, N., Katsuda, T., Kato, T., & Ochiya, T. (2013). Comparative
9 marker analysis of extracellular vesicles in different human cancer types. *J Extracell*
10 *Vesicles*, *2*. doi:10.3402/jev.v2i0.20424
- 11 Zamanian, J. L., Xu, L., Foo, L. C., Nouri, N., Zhou, L., Giffard, R. G., & Barres, B. A. (2012).
12 Genomic analysis of reactive astrogliosis. *J Neurosci*, *32*(18), 6391-6410.
13 doi:10.1523/JNEUROSCI.6221-11.2012
- 14 Zhao, Z. H., Chen, Z. T., Zhou, R. L., Zhang, X., Ye, Q. Y., & Wang, Y. Z. (2018). Increased DJ-
15 1 and alpha-Synuclein in Plasma Neural-Derived Exosomes as Potential Markers for
16 Parkinson's Disease. *Front Aging Neurosci*, *10*, 438. doi:10.3389/fnagi.2018.00438
- 17 Zorita, E., Cusco, P., & Fillion, G. J. (2015). Starcode: sequence clustering based on all-pairs
18 search. *Bioinformatics*, *31*(12), 1913-1919. doi:10.1093/bioinformatics/btv053

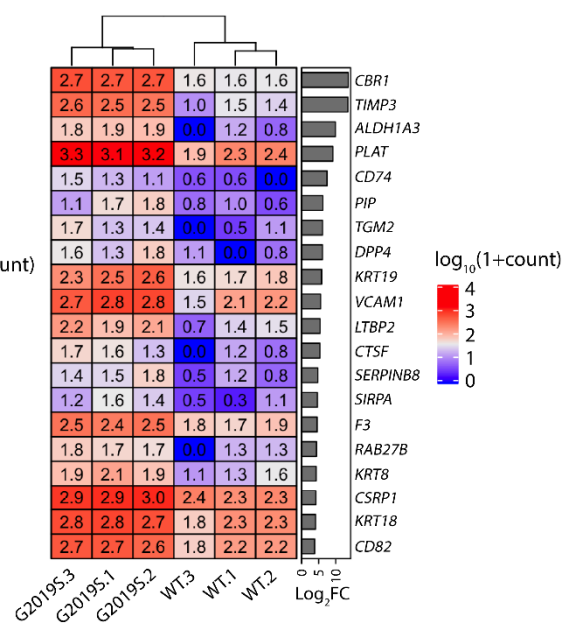
A



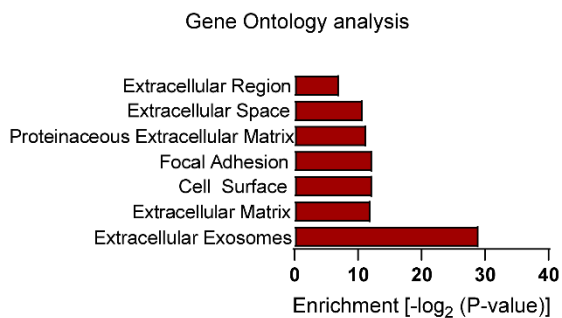
B



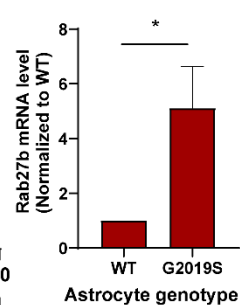
C



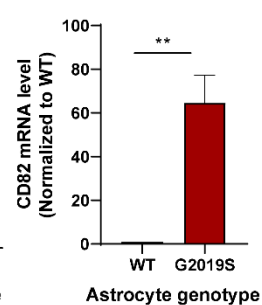
D



E



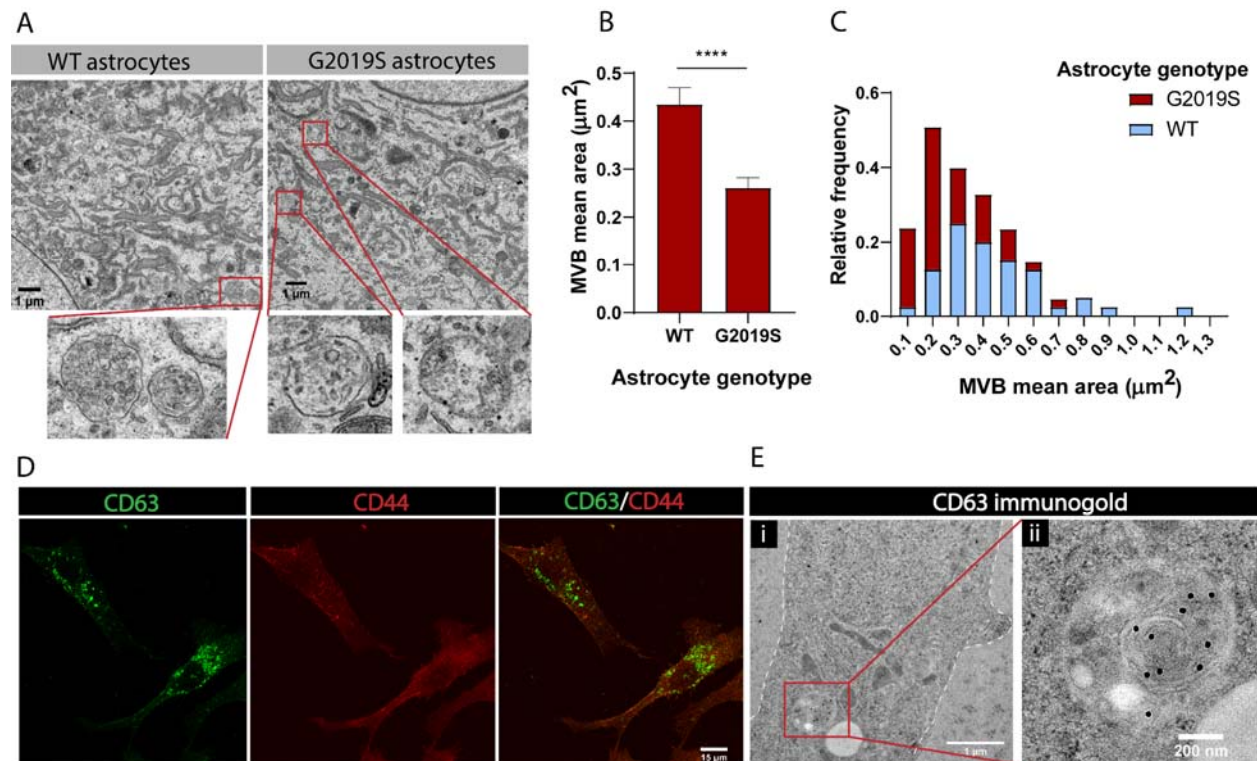
F



1

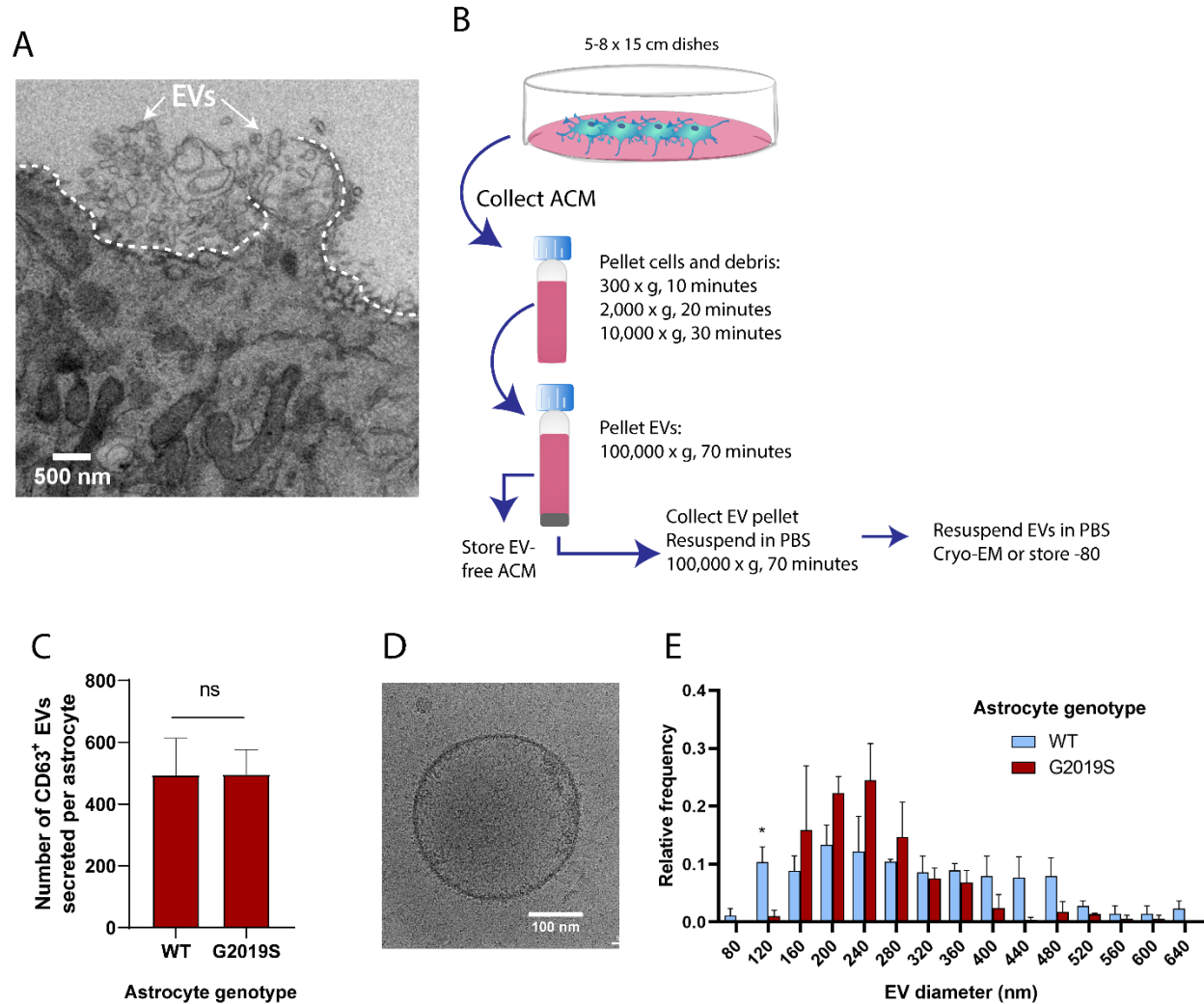
2 **Figure 1. Expression of exosome components is dysregulated in LRRK2 G2019S**
 3 **astrocytes.** (A) Astrocytes were prepared from iPSCs carrying the PD mutation LRRK2
 4 G2019S or its isogenic control. Confocal images of immunostained iPSC-derived astrocytes

1 show expression of astrocyte markers GFAP (green), vimentin (red), merged GFAP (green) and
2 vimentin (red) with the nuclear marker DAPI (blue), and merged astrocyte marker CD44 (red)
3 with DAPI (blue). (B) Heatmap representing the hierarchical clustering of significantly
4 upregulated and downregulated genes in LRRK2 G2019S vs WT astrocytes using a 1.4-fold
5 threshold for up-regulated genes and a 0.7-fold threshold for down-regulated genes, and a false
6 discovery rate of 0.05. Sequencing counts were normalized using the median of ratios method
7 and calculated by the EBseq package in R, as described in Materials and Methods, then
8 transformed using $\log_{10}(1+\text{normalized sequencing counts})$. The genes are separated into three
9 categories based on their $\log_{10}(1+\text{normalized sequencing counts})$ value using k-means
10 clustering with $k=3$ to reveal groups of low, moderate or high expression genes. Genes
11 encoding exosome-related components are indicated on the right (purple lines, with each
12 indicating one gene). (C) Heatmap representing the differential expression of 20 genes
13 encoding exosome components in WT and LRRK2 G2019S astrocytes, across three
14 independent biological replicates (labeled 1 to 3). The values represent the $\log_{10}(1+\text{normalized}$
15 $\text{sequencing counts})$ transformation as described in Materials and Methods, $\log_2\text{FC}$ represents
16 LRRK2 G2019S vs WT fold change in gene expression. Genes are sorted by their $\log_2\text{FC}$ value
17 in order of descending fold-change. (D) Gene ontology analysis of up-regulated genes identified
18 by RNA sequencing, and Benjamini-Hochberg adjusted P-values were obtained from the
19 Database for Annotation, Visualization and Integrated Discovery (DAVID) tool. (E, F) Gene
20 expression validation by qPCR of two exosome components, Rab27b (E) and CD82 (F). Data
21 are from four independent biological replicates; error bars represent mean + standard error of
22 the mean (SEM). Statistical analysis was performed using two-tailed unpaired Student's t-test
23 with equal standard deviation (s.d.) (* $p \leq 0.05$, ** $p < 0.01$).

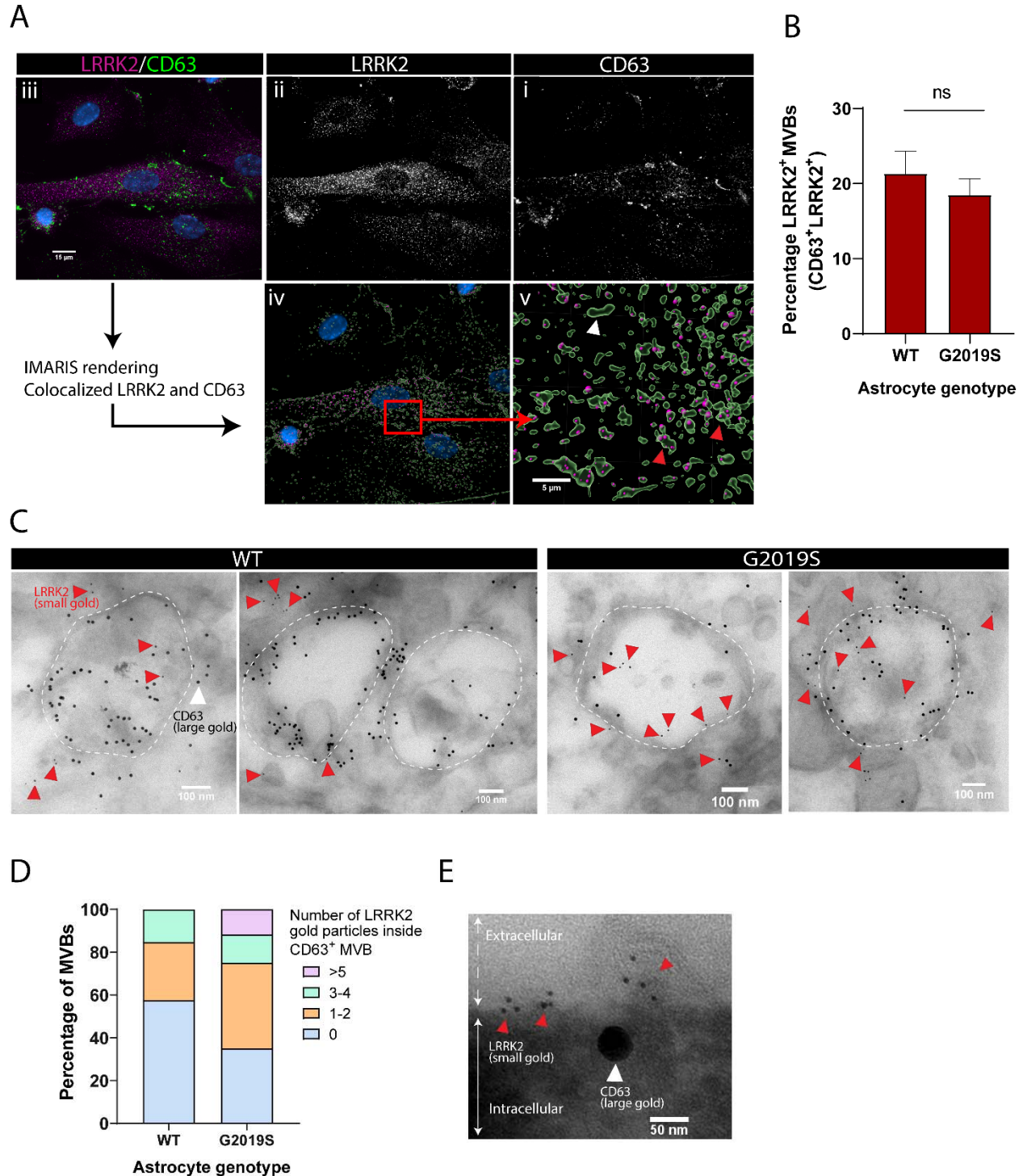


1
2 **Figure 2. MVBs in LRRK2 G2019S astrocytes are smaller than in WT astrocytes.** (A)
3 Transmission electron microscopy (TEM) images of multi vesicular bodies (MVBs) in WT and
4 LRRK2 G2019S astrocytes. For illustration purposes, the red boxes in the top panel indicate
5 MVBs in the cytoplasm of astrocytes and the lower panel shows a zoomed-in view of the MVBs.
6 (B, C) Quantification of mean area (B) and size distribution (C) of MVBs identified in TEM
7 images of WT and LRRK2 G2019S astrocytes. Data are sampled from at least 20 cells (≥ 40
8 MVBs) in each experimental condition; error bars represent mean + SEM for two independent
9 biological samples (B). Statistical analysis was performed using two-tailed unpaired Student's t-
10 test with equal s.d. (**** < p 0.0001). (D) Representative confocal images of astrocytes labeled
11 by immunofluorescence with the exosome marker CD63 (green) and the astrocyte marker CD44
12 (red). (E) Electron microscopy image showing immunogold labeling of CD63 (large gold) in
13 astrocytes. The dashed line delineates the astrocyte cell membrane (Ei). The red box indicates
14 an MVB, and the zoomed-in image shows CD63 gold particles inside an MVB (Eii).

15



1
2 **Figure 3. The size distribution of extracellular vesicles (EVs) secreted by astrocytes is**
3 **altered in the LRRK2 G2019S mutant.** (A) TEM images demonstrate that iPSC-derived
4 astrocytes actively produce and secrete EVs by exocytosis. The dashed line delineates the
5 plasma membrane. The white arrows indicate EVs. (B) Overview of the procedure to isolate
6 EVs by ultracentrifugation. ACM: astrocyte conditioned medium, Cryo-EM: cryogenic electron
7 microscopy. (C) Quantification of the number of CD63⁺ EVs secreted in WT and LRRK2
8 G2019S ACM by ELISA, using ELISA standards calibrated by nanoparticle tracking analysis as
9 discussed in Materials and Methods. Data are from at least three independent biological
10 replicates; error bars represent mean + SEM. Statistical analysis was performed using two-
11 tailed unpaired Student's t-test with equal s.d. (ns: not significant). (D, E) Secreted EVs were
12 imaged by cryo-EM (D) and their diameter was measured (E). Data are from ≥ 177 EVs isolated
13 from ACM taken from 30.4×10^6 plated astrocytes for each experimental condition; error bars
14 are mean + SEM for three independent biological replicates. Statistical analysis was performed
15 using two-tailed unpaired Student's t-test with equal s.d. (* $p \leq 0.05$).

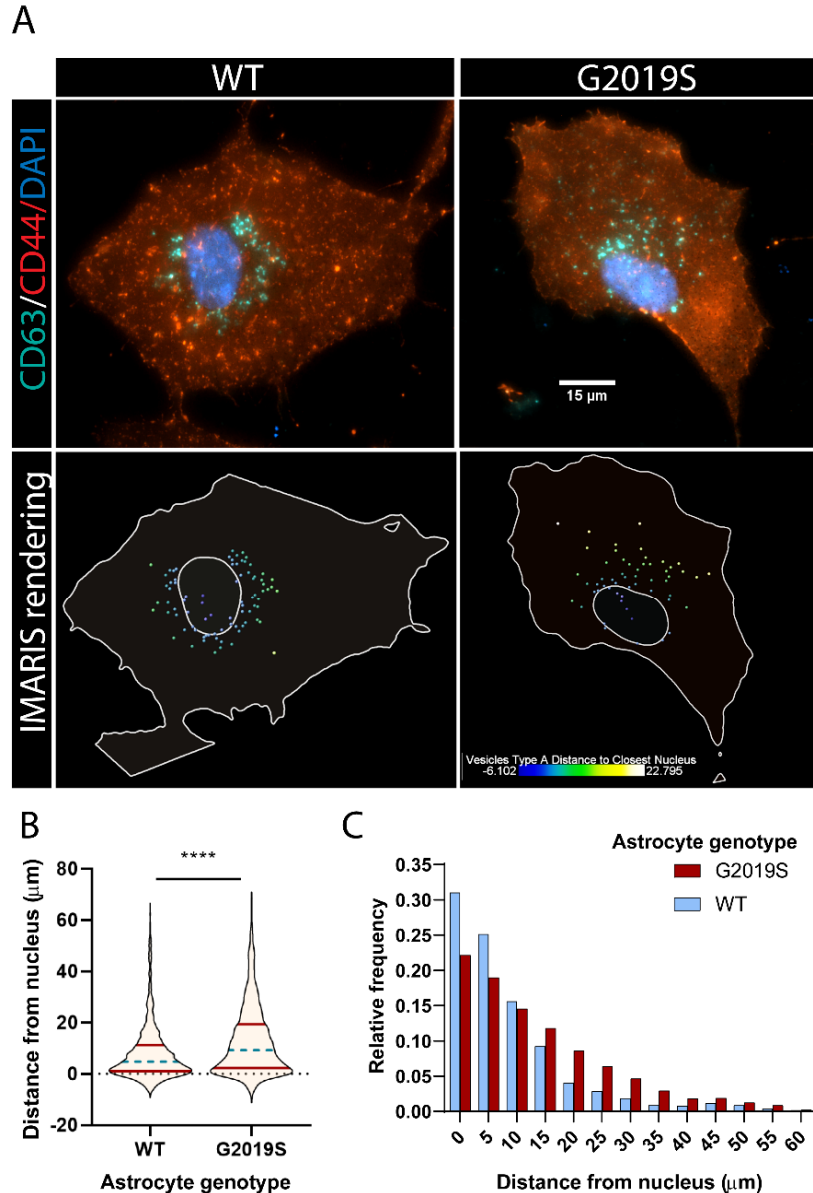


1

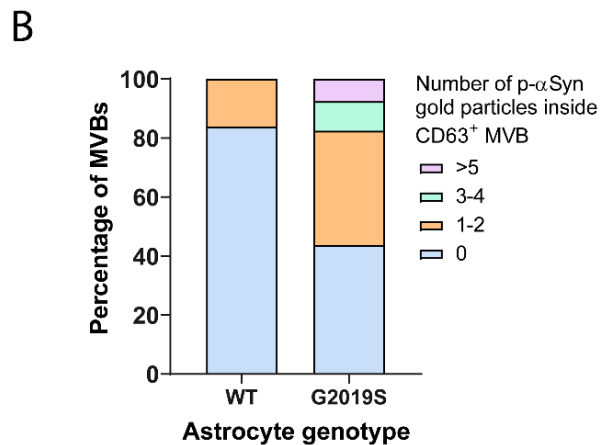
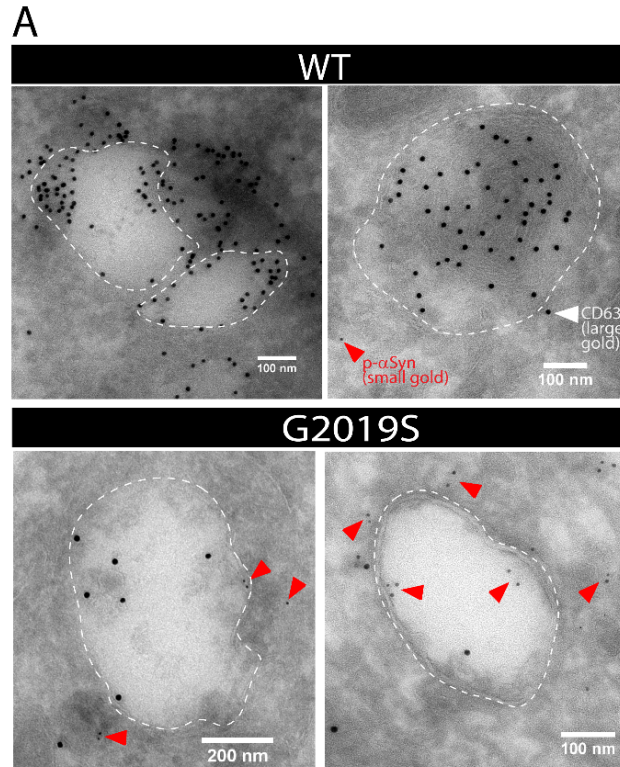
2 **Figure 4. LRRK2 is associated with MVBs in astrocytes and accumulates in the MVBs of**
 3 **LRRK2 G2019S mutant.** (A) Representative images of astrocytes labeled by
 4 immunofluorescence with CD63 (Ai), LRRK2 (Aii), and merged CD63 (green), LRRK2 (purple)
 5 and the nuclear marker DAPI (blue) (Aiii). The images were analyzed using IMARIS software to
 6 identify CD63⁺ MVBs (green surfaces) colocalized with LRRK2 (purple dots), and show the
 7 localization of the nucleus (DAPI, blue) (Aiv). A zoomed-in image shows two populations of

1 CD63⁺ surfaces: CD63⁺/LRRK2⁺ (red arrowhead), and CD63⁺/LRRK2⁻ (white arrowhead) (Av).
2 (B) Percentage of CD63-labeled surfaces that are also LRRK2 positive in WT and LRRK2
3 G2019S astrocytes, quantified with Imaris software using object-based colocalization. Data are
4 from three independent biological replicates, and ≥ 40 astrocytes ($> 3,000$ MVBs) were
5 analyzed per experimental condition; error bars represent mean + SEM. Statistical analysis was
6 performed using two-tailed unpaired Student's t-test with equal s.d. (ns: not significant). (C)
7 Immunogold electron microscopy shows the presence of LRRK2 (small gold, red arrowheads)
8 inside and in the vicinity of CD63⁺ MVBs (large gold) in WT and LRRK2 G2019S astrocytes.
9 The dashed lines indicate the contour of MVBs. (D) Distribution of CD63⁺ MVBs according to
10 their number of internal LRRK2 gold particles. Data are sampled from at least 20 astrocytes (\geq
11 59 MVBs) in each experimental condition. The distribution is significantly different in LRRK2
12 G2019S astrocytes compared to WT astrocytes (P-value = 0.0084, Chi-square test). (E)
13 Immunogold electron microscopy shows the secretion of LRRK2 (small gold, red arrowheads)
14 and EVs from a CD63⁺ MVB (large gold, white arrowhead). The dashed line indicates the
15 extracellular compartment, the solid line indicates the intracellular compartment.

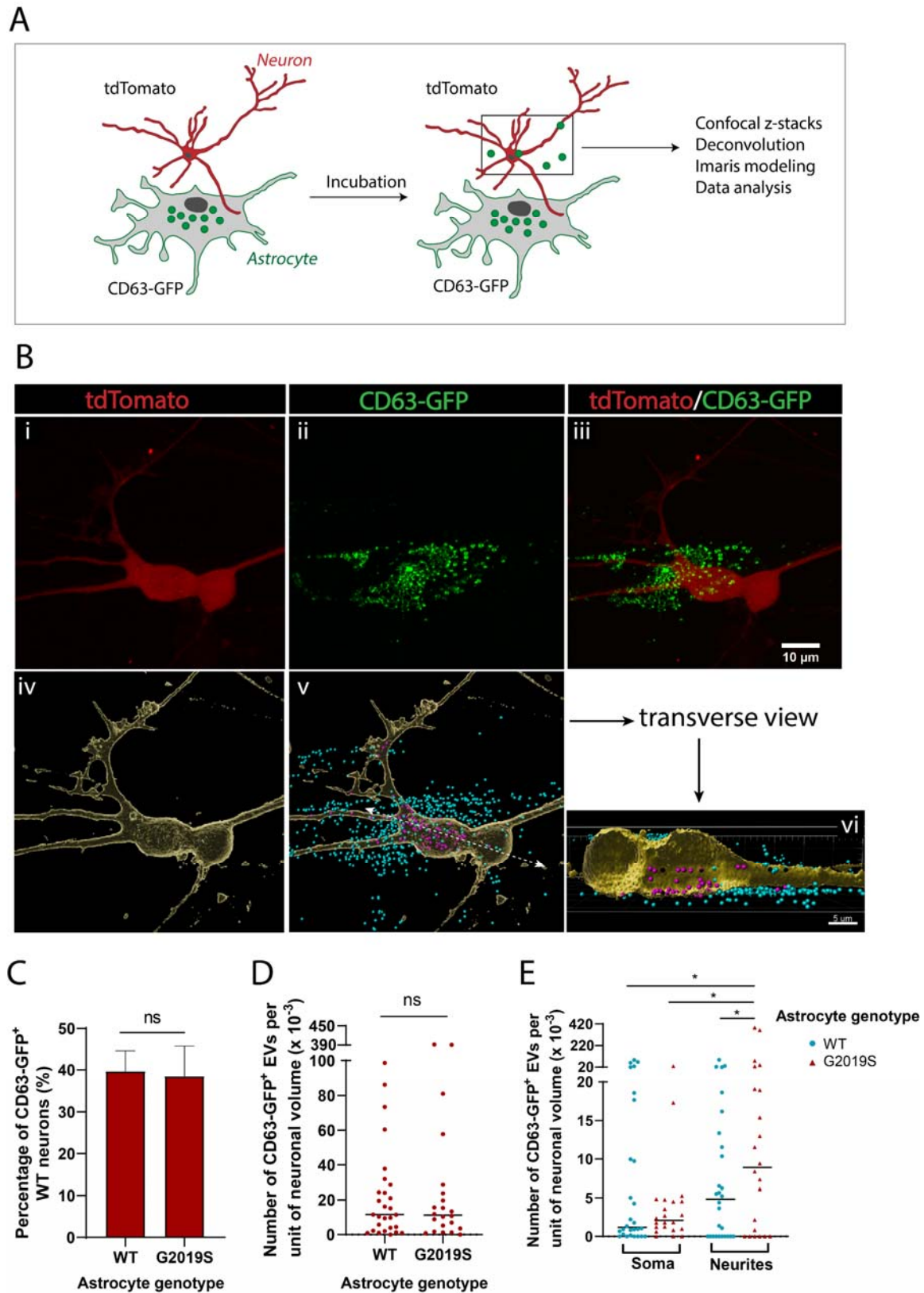
16



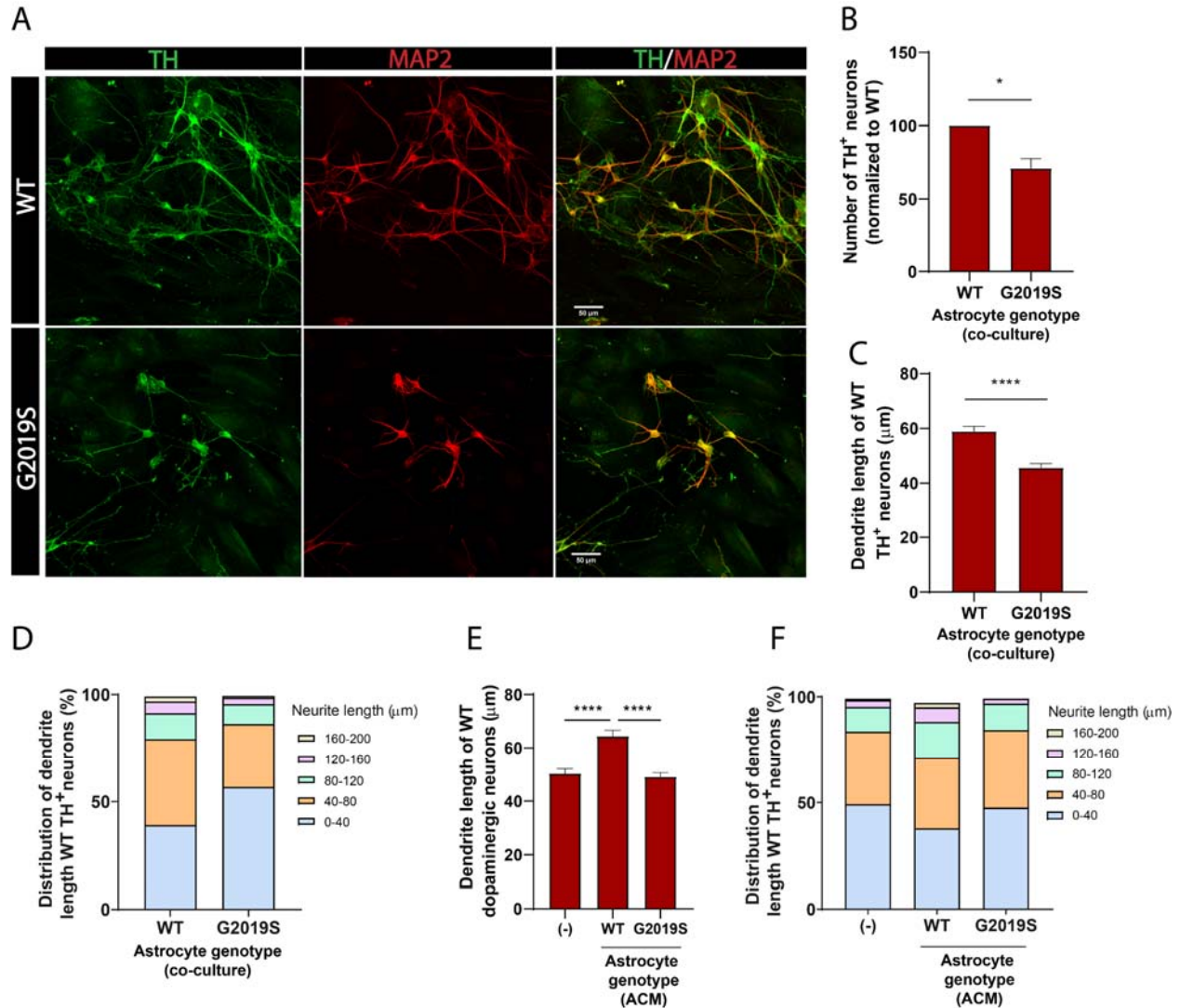
1
2 **Figure 5. The spatial distribution of MVBs in LRRK2 G2019S astrocytes is altered.** (A)
3 Representative immunofluorescence images of WT and LRRK2 G2019S astrocytes labeled with
4 the exosome marker CD63 (green), the astrocyte marker CD44 (red) and the nuclear marker
5 DAPI (dark blue). The bottom images show the corresponding IMARIS software rendering of
6 CD63⁺ MVBs, color-coded by distance to the nucleus, from blue (closest) to white (farthest).
7 The plain white lines indicate the cell boundary (outer line) and nucleus (inner circle). (B, C)
8 Quantification of the distance of CD63⁺ MVBs from the nuclear membrane in WT and LRRK2
9 G2019S astrocytes using IMARIS software “vesicles distance to closest nucleus” calculation.
10 The violin plot shows the median (blue dashed line) and interquartile range (red solid line) (B).
11 Data are from three independent biological replicates, 40-70 astrocytes (> 3,300 MVBs) were
12 analyzed for each experimental condition. Statistical analysis was performed using a Mann-
13 Whitney test (**** $p < 0.0001$).



1
2 **Figure 6. Alpha-synuclein and phospho-S129 alpha-synuclein are associated with MVBs**
3 **in astrocytes and accumulate in the MVBs of LRRK2 G2019S mutant.** (A) Immunogold
4 labeling of phospho-S129 alpha-synuclein (p- α Syn, small gold, red arrowheads) and CD63
5 (large gold) shows localization of p- α Syn inside and in the vicinity of MVBs in astrocytes. The
6 low abundance of small gold particles in the control sample is consistent with the observation
7 that healthy brain tissues contain low levels of p- α Syn (Fujiwara et al., 2002). The dashed lines
8 indicate the boundary of the MVBs. (B) Distribution of CD63⁺ MVBs according to their number of
9 internal p- α Syn gold particles, in WT and LRRK2 G2019S astrocytes. Data are sampled from at
10 least 20 astrocytes (30-79 MVBs) for each experimental condition. The distribution is
11 significantly different in LRRK2 G2019S astrocytes compared to WT astrocytes (P-value =
12 0.0014, Chi-square test).

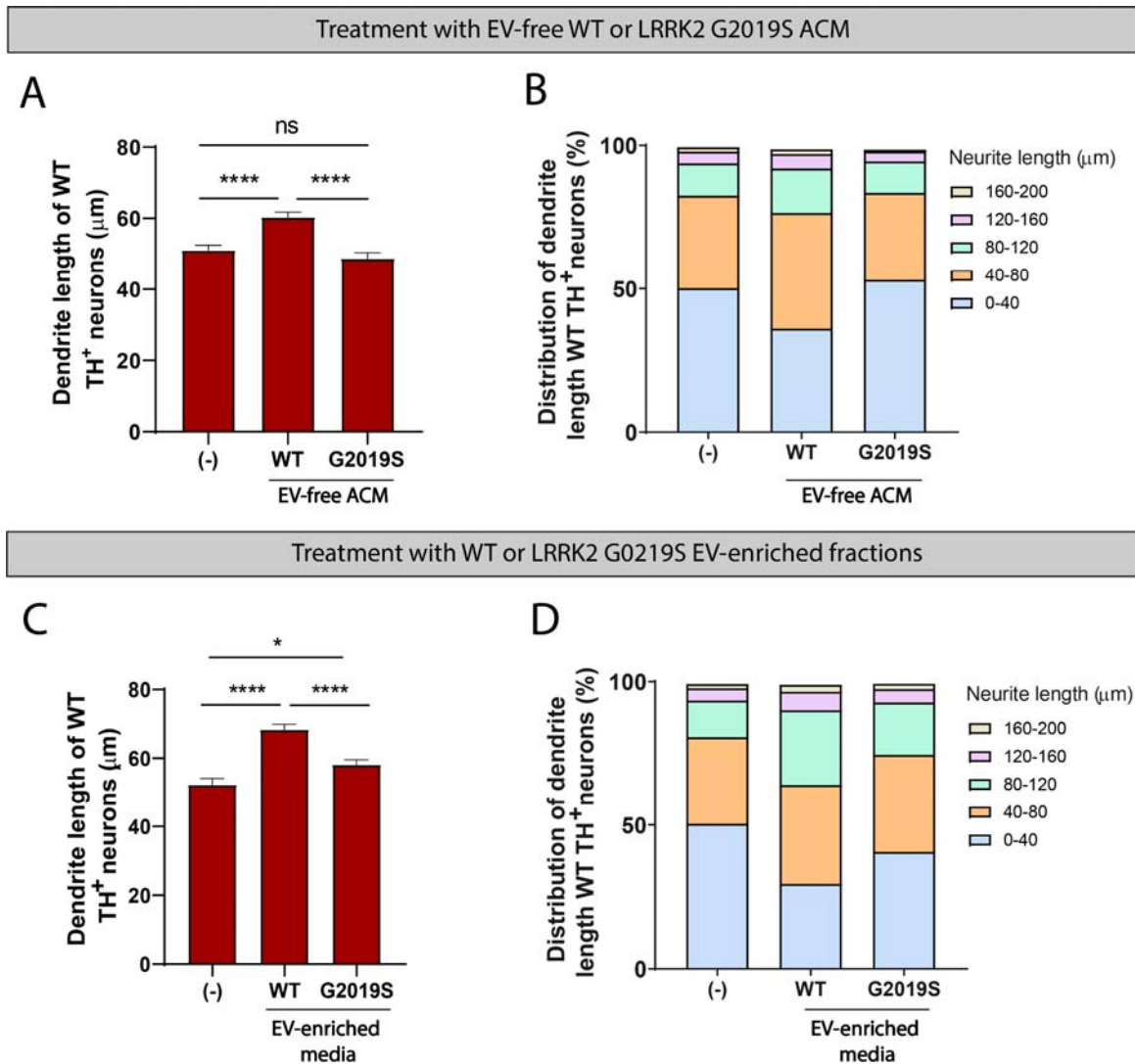


1 (red), and WT or LRRK2 G2019S astrocytes were transduced with lenti-CD63-GFP (green) to
2 produce green-labeled exosomes. Neurons and astrocytes were co-cultured, and uptake of
3 CD63-GFP exosomes by neurons was monitored by live-cell confocal microscopy, followed by
4 deconvolution and Imaris modeling. (B) Confocal images of tdTomato neurons (Bi), CD63-GFP
5 astrocytes (Bii) and the merged image (Biii). The corresponding IMARIS software rendering
6 represents tdTomato neurons in yellow (Biv), and the CD63-GFP exosomes in blue (outside the
7 neurons) or purple (inside the neurons) (Bv). A transverse view of a neuron shows purple-
8 labeled exosomes inside the somas and neurites (Bvi). (C) Quantification of the percentage of
9 neurons with internalized WT or LRRK2 G2019S CD63-GFP exosomes at the time of live-cell
10 imaging. (D) Quantification of the number of CD63-GFP exosomes per unit of neuronal volume.
11 (E) Quantification of the number of CD63-GFP exosomes per unit of soma or neurite volume.
12 For all datasets: data are from three independent biological replicates, ≥ 80 neurons were
13 analyzed for each experimental condition. The scatter plot shows the median value. Statistical
14 analysis was performed using two-tailed unpaired Student's t-test with equal s.d. (C, D), or one-
15 way ANOVA with Newman-Keuls multiple comparisons (E) (ns: not significant, * $p \leq 0.05$).



1
2 **Figure 8. LRRK2 G2019S astrocytes affect the viability and morphology of dopaminergic**
3 **neurons.** (A) Confocal images showing neurons labeled by immunofluorescence with the pan-
4 neuronal and dendrite marker MAP2 (red), the marker for dopaminergic neurons TH (green),
5 and the merged image (MAP2, red and TH, green). MAP2: microtubule-associated protein 2,
6 TH: tyrosine hydroxylase. (B-D) Quantification of neuron viability (number of dopaminergic
7 neurons remaining in culture) (B), average dendrite length (C), and dendrite length distribution
8 (D) after 14 days in culture with WT or LRRK2 G2019S astrocytes. Viability data are from five
9 independent biological replicates, and an average of 810 WT and 530 LRRK2 G2019S neurons
10 were counted (B). Dendrite length data are from three independent biological replicates, and
11 more than 500 neurites were measured for each experimental condition (C-D). (E-F) WT
12 dopaminergic neurons were cultured for 14 days with basal medium (-), WT or LRRK2 G2019S
13 ACM, and the resulting dendrite length average (E) and distribution (D) were quantified. The
14 data are from three independent biological replicates, and more than 450 neurites were
15 measured per experimental condition. For all datasets, error bars represent mean + SEM (B, C,
16 E); statistical analysis was performed using two-tailed unpaired Student's t-test with equal s.d.
17 (B, C) or one-way ANOVA with Tukey's multiple comparisons correction (E) (* $p \leq 0.05$, ****

- 1 p<0.0001). Results shown in panel B support similar observations recently documented in a
- 2 non-isogenic model system (di Domenico et al., 2019).



1
2 **Figure 9. WT but not LRRK2 G2019S astrocytes release neurotrophic factors via two**
3 **distinct secretory pathways to support the growth of dopaminergic neurons.** (A, B)
4 Quantification of the average (A) and distribution (B) of dendrite lengths of WT dopaminergic
5 neurons cultured for 14 days with basal medium (-), or WT or LRRK2 G2019S EV-free ACM.
6 Data are from four independent biological replicates, and ≥ 650 neurites were measured for
7 each experimental condition. (C, D) Quantification of the average (C) and distribution (D) of
8 dendrite lengths of WT dopaminergic neurons cultured for 14 days with basal medium (-), or WT
9 or LRRK2 G2019S EV-enriched fractions. Data are from three independent biological replicates,
10 and ≥ 450 dendrite were measured for each experimental condition. Error bars represent mean
11 + SEM (A, C), and statistical analysis was performed using one-way ANOVA with Tukey's
12 multiple comparisons correction (ns: not significant, * $p \leq 0.05$, **** $p < 0.0001$).

13

1 **The LRRK2 G2019S mutation alters astrocyte-to-neuron communication via**
2 **extracellular vesicles and induces neuron atrophy in a human iPSC-derived**
3 **model of Parkinson's disease**

4

5 Aurelie de Rus Jacquet^{1*}, Jenna L. Tancredi¹, Andrew L. Lemire¹, Michael C. DeSantis¹, Wei-
6 Ping Li¹, Erin K. O'Shea^{1*}

7

8 ¹Janelia Research Campus, Howard Hughes Medical Institute, Ashburn, VA, 20147

9 *Co-corresponding authors: Aurelie de Rus Jacquet : aureliederus@gmail.com; Erin O'Shea :
10 osheae@hhmi.org

11

12

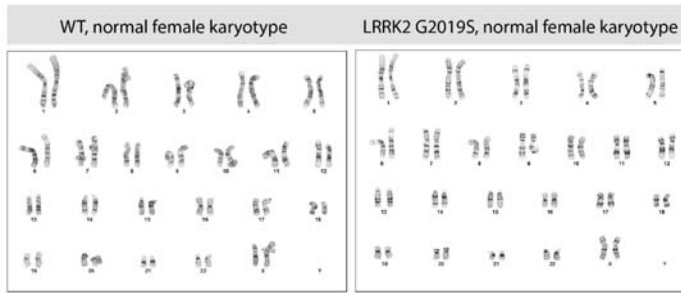
13 **Supplementary Files**

14

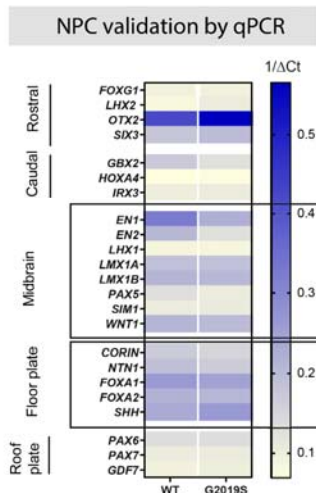
15

16

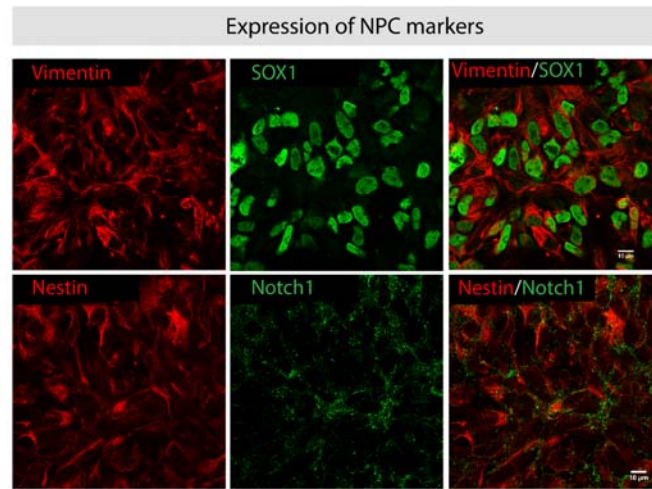
A



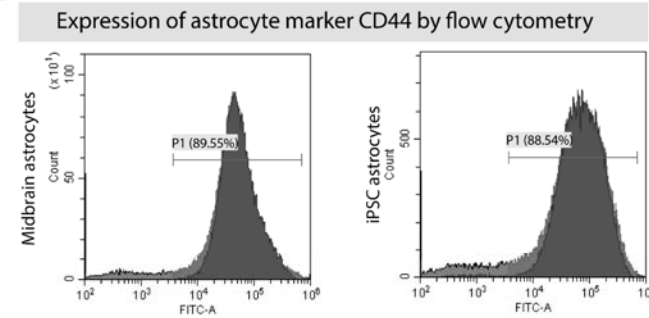
B



C

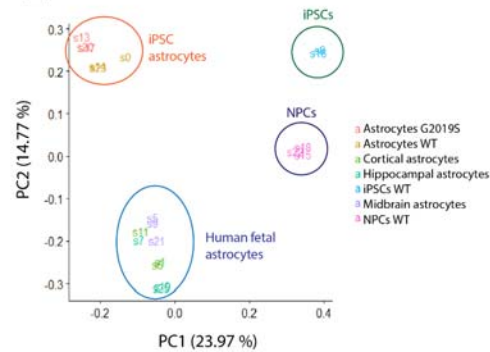


D

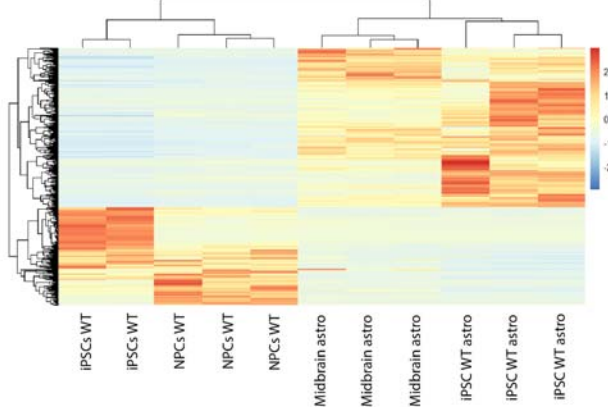


Validation of iPSC-derived NPC and astrocyte transcriptomic signature and identity

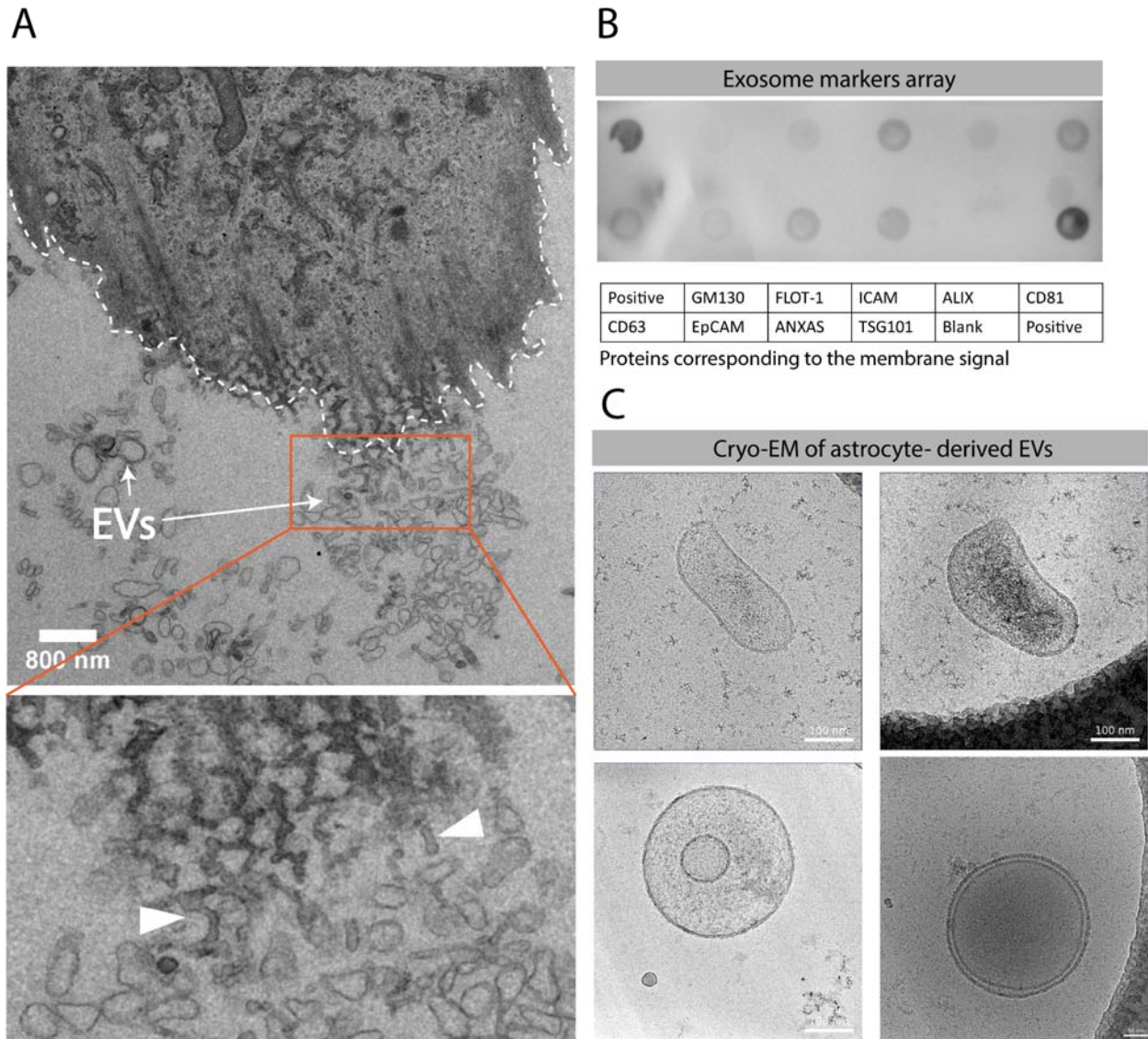
E



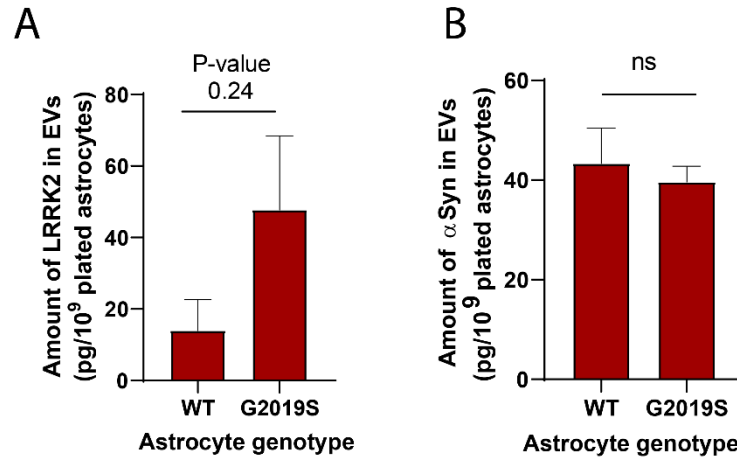
F



1 **Supplementary Figure 1. Quality control of iPSCs and iPSC-derived cell types.** (A) Normal
2 human female karyotype prepared from WT and LRRK2 G2019S iPSCs. Cytogenetic analysis
3 was performed on 20 G-banded metaphase cells for each genotype. (B) Representative
4 heatmap showing the gene expression profile of NPCs patterned towards a midbrain fate. The
5 left side of the heatmap identifies gene markers for specific brain regions (Kirkeby et al., 2012).
6 Successfully differentiated NPCs should show higher expression levels of genes shown in the
7 two black boxes (midbrain and floor plate) compared to other genes (Kirkeby et al., 2012; Kriks
8 et al., 2011). The scale is calculated based on the $1/\Delta$ cycle threshold (Ct) values calculated
9 from the Ct of the gene of interest compared to the Ct of the loading control β -actin. (C)
10 Confocal images of immunostained NPCs show expression of NPC markers vimentin (red),
11 SOX1 (green), and merged vimentin (red) and SOX1 (green). The lower panel shows the
12 expression of the markers nestin (red), notch1 (green), and merged nestin (red) and notch1
13 (green). (D) Histogram representing the proportion of astrocytes expressing the marker CD44
14 by flow cytometry in cultures prepared from human fetal midbrain astrocytes (89.55 % CD44⁺
15 cells) or iPSC-derived astrocytes (88.54 % CD44⁺ cells). A total of 10,000 events were recorded
16 for each experimental condition. (E, F) To confirm the successful differentiation of iPSCs into
17 specific cell types, we performed RNA-seq of iPSCs, NPCs, iPSC-derived astrocytes and
18 human fetal astrocytes. RNA-seq data was analyzed by principal component analysis (PCA) (E)
19 and a heatmap representing the unsupervised cluster analysis was generated (F); data are from
20 two (iPSCs) or three (NPCs, iPSC-derived astrocytes and fetal astrocytes) independent
21 biological replicates.

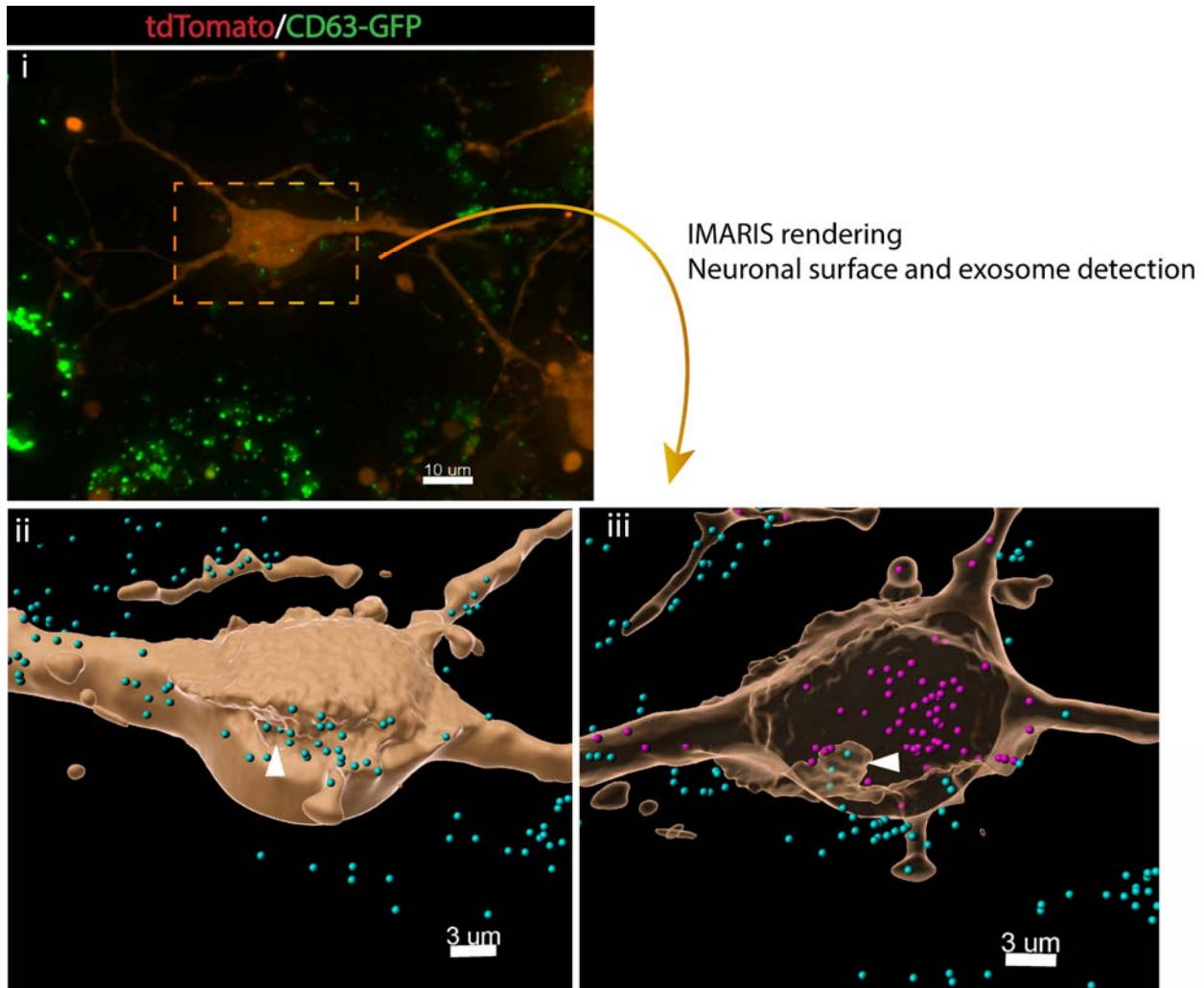


Supplementary Figure 2. Analysis of astrocyte-secreted EVs. (A) TEM image of an astrocyte and astrocyte-secreted EVs. The dashed line indicates the astrocyte cell membrane, and the arrows indicate EVs. The red box and the zoomed-in view show EVs that appear to bud from the astrocyte membrane (white arrowheads). (B) Identification of exosome markers in EV-enriched fractions obtained from ACM using an exosome antibody array. Each circle on the membrane represents a pre-printed antibody spot marker of exosome or cellular contaminant, and the table details the name of each antibody marker spotted on the membrane. (C) Cryo-EM images of astrocyte-derived EVs that display an unusual morphology.



1
2

3 **Supplementary Figure 3. Presence of PD-related proteins in astrocyte-derived EVs.** (A)
4 Quantification of the amount of LRRK2 in WT or LRRK2 G2019S EV-enriched fractions by
5 ELISA. Data are from at least three independent biological replicates. (B) Quantification of the
6 amount of alpha-synuclein (αSyn) in WT and LRRK2 G2019S EV-enriched fractions by ELISA.
7 Data are from seven independent biological replicates. For all datasets, error bars represent
8 mean + SEM; statistical analysis was performed using two-tailed unpaired Student's t-test with
9 equal s.d. (ns: not significant).



1

2

3 **Supplementary Figure 4. Dopaminergic neurons internalize astrocyte-derived EVs by**
4 **endocytosis.** Widefield image of co-cultured tdTomato neurons (red) and CD63-GFP
5 astrocytes (green) (4i). The dashed red box shows the neuronal soma, and the corresponding
6 IMARIS software rendering represents the tdTomato neuron in yellow (4ii, 4iii), and the CD63-
7 GFP EVs in blue (outside the neurons) or purple (inside the neurons). The white arrowhead
8 shows the internal budding of the neuronal plasma membrane and endocytosis of extracellular
9 CD63⁺ exosomes.

10